# Internal Solitary Waves in the Warm Pool of the Western Equatorial Pacific

ROBERT PINKEL

*Marine Physical Laboratory, Scripps Institution of Oceanography, La Jolla, California*

(Manuscript received 29 June 1999, in final form 7 January 2000)

ABSTRACT

During the spring tides of late November 1992, early January and early February 1993, solitary internal wave packets were observed at 2°S, 156°15′E in the western equatorial Pacific. Apparently generated in the Nuguria island group (3°S, 153°E), the waves propagate northeastward at 2.4–2.8 m $s^{-1}$, appearing in fixed phase with the underlying semidiurnal baroclinic tide. The initial solitary wave crests have downward displacements in excess of 60 m and peak velocities greater than 80 cm $s^{-1}$. Groups of 1–3 crests are observed, with vertical structure resembling a first-mode internal wave and horizontal variability consistent with third-order comb KdV solitons. Many of the packets exhibit an overall organization reminiscent of undular bores. This borelike behavior is confined primarily to the upper 70 m, not sharing the mode-one dependency of the crests. The solitons displace the ambient equatorial currents, including the Equatorial Undercurrent, both vertically (80 m), and laterally (1–2 km), with little apparent interaction.

A 161-kHz Doppler sonar mounted on the R.V. *John Vickers* provided ocean velocity measurements with 3-m vertical resolution and 2-min time resolution in the upper 250 m of the sea. Merged with GPS-derived ship's navigation, the resultant depth–time records of absolute velocity enable estimation of flow streamlines, given the two-dimensional nature of the wave trains. During passage of the soliton crests, the vertical displacement of streamlines is in good agreement with the observed vertical displacement of biological scattering layers.

Noticeable increases in acoustic scattering strength are associated with the passage of all soliton groups, suggesting the (turbulent) production of small-scale (0.46 cm) structure in the sound speed field. However, the shear in these mode-one solitons is small compared to ambient equatorial background shears. The minimum Richardson number intrinsic to the soliton packet is of order 15. The crests apparently trigger small-scale instabilities on the background shear. Several of the soliton packets display pronounced internal wave ''tails.'' These too are apparently triggered disturbances on the preexisting flow. High-frequency shears are oriented nearly orthogonal to the low-frequency background, independent of the propagation direction of the soliton.

The energy density of the larger soliton groups approaches 0.2 gigajoules per meter of crest, a value comparable to the underlying baroclinic tide, and also comparable to the energy lost from the $M_2$ barotropic tide over a ~1500 km propagation path through the western tropical Pacific (given a mean barotropic dissipation rate of $3 \times 10^{-3}$ W $m^{-2}$ for the region).

## 1. Introduction

Some of the warmest surface waters in the world are found in the western equatorial Pacific. Temperatures in excess of 28°C occur from the date line westward into the Indian Ocean in a band roughly ±10° about the equator. The strong surface heating of the region, with attendant evaporation, provides driving impetus to the large-scale atmospheric circulation. Fluctuations in the state of this so-called warm pool are associated with subsequent oceanic and atmospheric fluctuations eastward along the equator and throughout the Pacific basin.

To investigate the physics of this region a multinational air–sea interaction experiment, Tropical Ocean Global Atmosphere Comprehensive Ocean–Atmosphere Response Experiment (TOGA COARE), was conducted during 1992–93 (Webster and Lukas 1992). The COARE Intensive Observing Period (IOP) was fielded during the boreal winter of 1992/93. Three aircraft, 17 ships, and hundreds of people assembled in the region in an attempt to document the local heat budget.

At the time of COARE, it was not appreciated that the warm pool was also significant as a dissipation region for the $M_2$ barotropic tide. Subsequent TOPEX/Poseidon measurements indicate that as much as 90 GW of tidal energy is dissipated in the broad region stretching from the Solomon Islands northward over the Ontong–Java Plateau to the equator and eastward through the central South Pacific (Egbert 1997, his region 6). Independent modeling studies indicate the region is also a source for baroclinic internal tides (Sjoberg and Stigebrandt 1992; Morozov 1995). From a synthesis of direct observations, Feng et al. (1998, henceforth F98)

*Corresponding author address:* Dr. Robert Pinkel, Scripps Institution of Oceanography/MPL, 9500 Gilman Drive, Mail Code 0213, La Jolla, CA 92093-0213.
E-mail: rpinkel@ucsd.edu

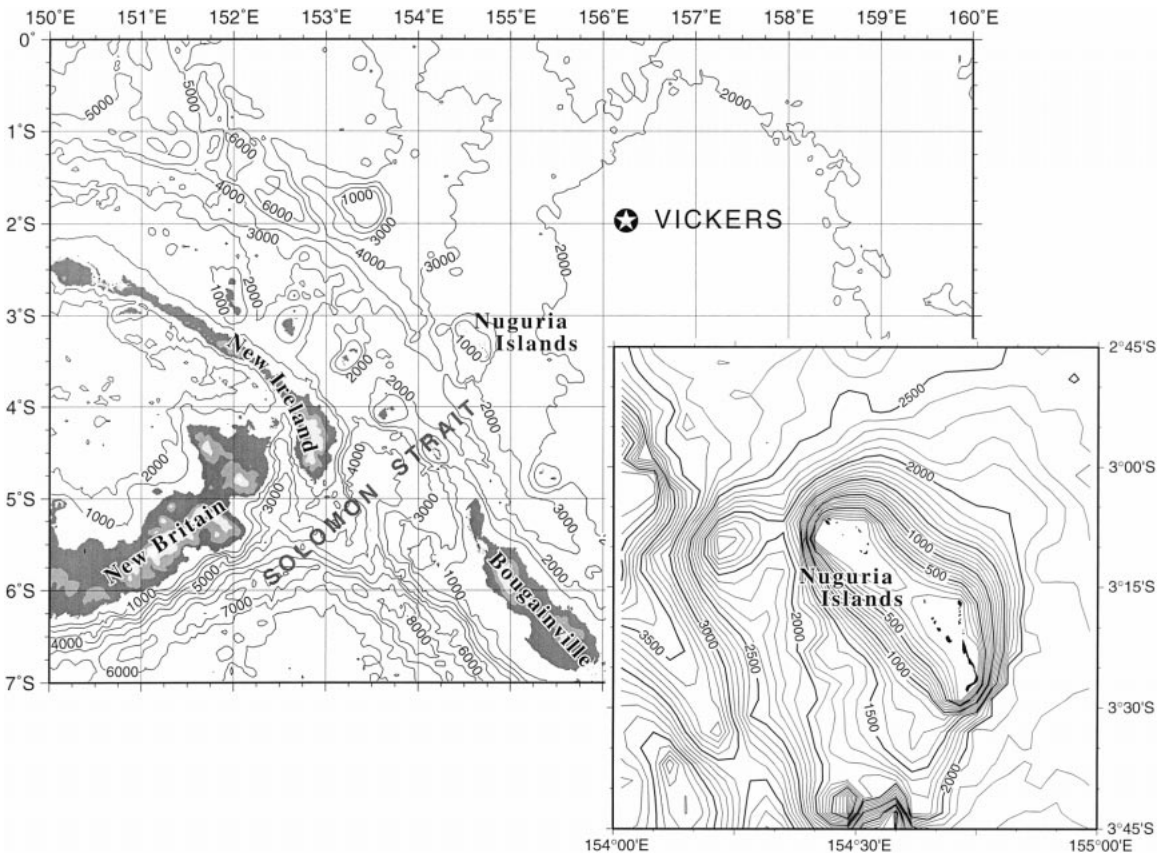


FIG. 1. (a, b) Seafloor topography of the western equatorial Pacific. The inset is a close-up of the Nuguria Islands, a suspected generation site.

report 538 W $m^{-1}$ (0.5 gW across a 1000-km wave front) radiating northeastward in the mode-one baroclinic tide. Gourdeau (1998), using Topex observations and a 6-month record of mooring data, confirms F98 and notes that 59% of the semidiurnal variation in surface dynamic height is found in the combined $M_2$, $S_2$, and $N_2$ tidal bands.

Tidal concerns were brought to the attention of COARE investigators with the sighting of numerous large amplitude (~80 m) nonlinear waves, propagating toward the northeast through the COARE Intensive Flux Array (centered at 2°S, 156°E; Fig. 1). A variety of phenomena, including distortion of baroclinic tidal crests, solitons, and borelike flows were observed. The solitons are similar to those sighted in the Andaman and Sulu Seas (Osborne and Burch 1980; Apel et al. 1985). These, however, appear to evolve as a deformation of the freely propagating internal tide (e.g., Gerkema and Zimmerman 1995; Pinkel et al. 1997), rather than developing from an arbitrary energetic disturbance (e.g., Lee and Beardsley 1974; Liu et al. 1985). A borelike aspect of these motions is often seen, as recently emphasized by Henyey and Hoering (1997). However, given the periodic nature of the phenomenon, the borelike ''aftermath'' of soliton passage is itself linked to the underlying tide. Indeed, the bore is manifest as an extremely skewed tidal waveform.

We present observations of these phenomena obtained during November 1992 through mid-February 1993 from the R.V. *John Vickers*. A profiling CTD; (during January), a high-resolution Doppler sonar (throughout), and a Global Positioning System (GPS) receiver provide estimates of the density and absolute velocity fields. Given the predominantly two-dimensional nature of the nonlinear waves and knowledge of the absolute velocity field, quantities such as sea surface elevation can be estimated directly from Newton's second law.

The COARE site and measurements are described briefly below, followed by an introduction to the observations. The energetics of the waves and their interaction with the larger environment of the warm pool are subsequently discussed.

## 2. Oceanographic background

The COARE Intensive Flux Array (IFA) was centered over the western edge of the Ontong–Java plateau. Water depth at the site is 1800 m. To the west and south, depth is highly variable, with 4-km water interspersed with

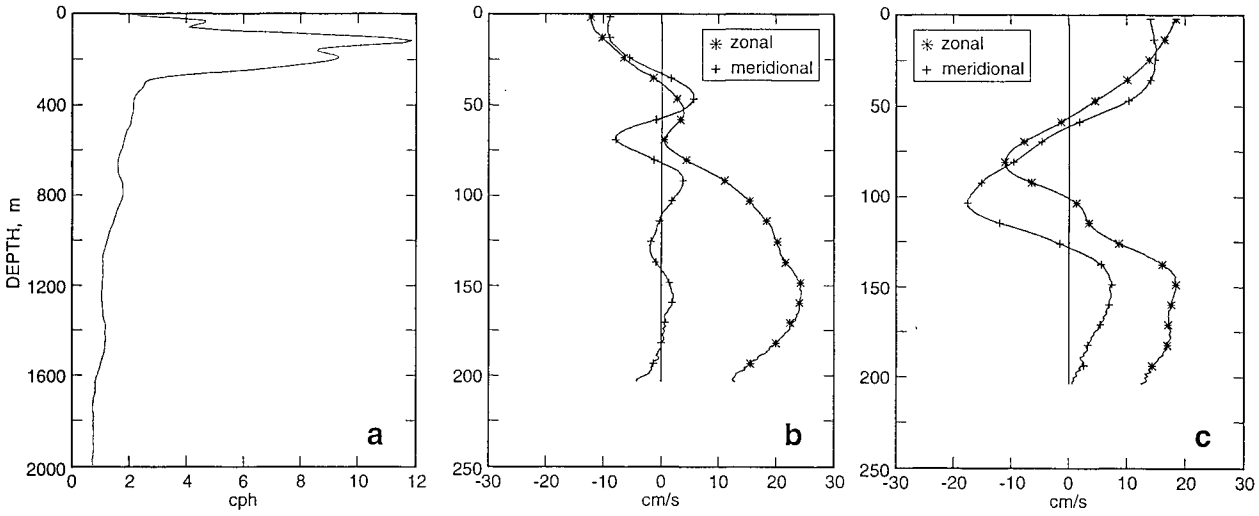


FIG. 2. A representative profile of buoyancy frequency for the COARE site (a). Vertical profiles of horizontal current averaged over 7–12 Jan (b) and 8–12 Feb (c), the periods when distinct nonlinear events are seen.

island chains such as the Solomons, New Guinea, and Indonesia (Figs. 1a,b).

The static stability of the water column, represented by the bouyancy frequency $N = [(g/\rho)\partial\rho/\partial z]^{1/2}$, where $g$ is gravitational acceleration, and $\rho$ is potential density, is presented in Fig. 2a. During COARE, the stability of the upper 90 m is highly variable. The top 30–40 m is frequently well mixed, with rain-freshened surface waters insulating the deeper mixed layer from mild atmospheric forcing (Lukas and Lindstrom 1991). Strong wind events, as well as intense baroclinic wave activity, occasionally break down this ''barrier,'' enabling exchange between the surface and the highly stratified waters at the mixed layer base. The stability of the water column peaks just below the mixed layer base, and again at 180–200 m ($N = 10$ cph), above the core of the undercurrent.

Throughout the COARE IFA, the barotropic semidiurnal tides are associated with primarily zonal flow, peaking at $\pm 5$ cm s$^{-1}$ during spring tides. Feng et al. (1998) report that the first-mode baroclinic tide propagates toward the northeast at 2.8 m s$^{-1}$, with a horizontal wavelength of 110 km. Maximum mode-one velocities are $\pm 7$ cm s$^{-1}$, aligned with the propagation direction. At the *Vickers* site, much higher velocities are seen, associated with the nonlinear deformation of the wave during spring tides.

Baroclinic horizontal velocities vary in depth as $N^{1/2}$ (Fofonoff 1969), while barotropic velocities are more nearly constant. The observed semidiurnal currents are primarily barotropic and zonal at depth (low $N$), and primarily baroclinic, oriented NE–SW in the high $N$ region above 150 m. In general, F98 report mode-two amplitudes to be 10% of mode-one. Both modes one and two are highly coherent with the astronomic forcing, suggesting local generation.

Of particular interest are the spring tides of 9–12 January and 7–12 February, when nonlinear wave activity is seen in the region. Ray et al. (1994) and Schrama and Ray (1994) have produced a global model of the semidiurnal tides based on TOPEX/Poseidon altimetric data. In the IFA, their model shows peak tidal elevations of $\pm 48$ and $\pm 58$ cm for these spring tides, in contrast to the $\pm 42$ cm maximum displacements during typical spring tides.

In an earlier 6-month record at the site, Gourdeau (1998) reports four sightings of nonlinear wave packets. These, also, are associated with spring tides that are marginally greater than the norm. Feng et al. report that at the IMET central mooring of the IFA (2°S, 156°E) peak mode-one baroclinic tides are also slightly greater than during typical spring tides. However, mode-two amplitudes grow to two (January) and five (February) times typical peak levels, with mode-two currents nearly as energetic as mode one during the early February spring period. The maximum spring mode-one tide lags its barotropic counterpart by approximately two days at the IMET site. Mode-two peaks four days after the barotropic maximum.

In addition to the tides, the westward-flowing South Equatorial Current (0∼150 m) and the southern flank of the Equatorial Undercurrent (150–250 m) occupy the site. A pronounced westerly wind burst (Weller and Anderson 1996) in late December forced the upper ocean initially eastward. Near-inertial ringing of ∼14–18-day period is seen for the remainder of the COARE IOP. Mean velocity profiles for the periods 7–12 January and 8–12 February are presented in Figs. 2b,c. These are formed as time averages at fixed depths. Substantial vertical excursions of the true low-frequency currents associated with tide and soliton passage serve to smooth these profiles significantly. Note that by early January, the near-inertial surface current has reversed. Surface flows are toward the southwest at 0.1 m s$^{-1}$. The Equa-

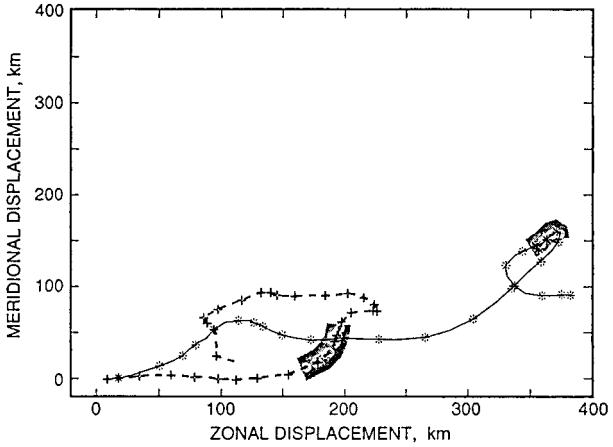


FIG. 3. Progressive vectors of surface currents, averaged over 10–40 m, at the *Vickers* site for the Dec–Jan (*) and Jan–Feb (+) *Vickers* deployments. The generally eastward currents have a pronounced inertial component. Mean surface currents are weakly toward the southwest (Jan) and toward the northeast (Feb) during observed event passage (shaded regions).

torial Undercurrent is shallow during this period, between 125 and 200 m.

A progressive vector presentation of surface currents is presented in Fig. 3. The rapid eastward advection following the December wind event is seen in the December–January record. Eastward surface advection diminishes in February, but the pronounced inertial signal remains. Solitons are seen during those spring tides when the zonal velocity of the upper 50 m is small.

## 3. Observations

In COARE, the R.V. *Vickers* maintained station at 2°S, 156°15′E. The primary function of the ship was to support an onboard meteorological radar that mapped rainfall rates over the IFA. This function was successfully performed in three phases, 11 November–12 December 1992, 20 December–15 January, and 20 January–18 February 1993, separated by port calls in Honiara, Guadalcanal.

Fortuitously, the *Vickers* station proved to be an ideal site to observe passage of the nonlinear waves. Indeed, the lateral displacements of the waves, of order 1 km, frequently swept the *Vickers* outside its mandated 15-km watch circle around the site. The February observations, in particular, were frequently marred by the ship's attempt to relocate, following the passage of soliton crests.

In addition to the radar and numerous meteorological sensors, a CTD and Doppler sonar provided a view of the upper ocean. The CTD, a Seabird SBE9, was operated at hourly intervals during Phases I and II, profiling to 150 m. During the wave events of early January 1993 it profiled continuously, to 150 m, every 12 min.

The Doppler sonar was constructed at the Marine Physical Laboratory of Scripps Institution of Oceanography. Four transducers, orthogonal in azimuth and 30° off vertical, were mounted on the hull adjacent to the ship's keel. Cylindrically symmetric acoustic beams of width ±3° (to the 3-dB points) were formed. The sonar transmitted a repeat sequence code (Pinkel and Smith 1992) consisting of five repeats of a four-bit code, with 0.25 ms/bit. The carrier frequency was 161 kHz. The nominal depth resolution of the sonar was 2.5 m. To realize this resolution, tilt corrections were applied in real time. The sonar was interfaced to a Datawell HIPPY model 120B vertical reference sensor, enabling averages of echo intensity and covariance to be formed at fixed depths, rather than fixed ranges. Two-minute averaged records were stored on magnetic disk.

The sonar profiled to depths of order 300 m while the ship was stationary. Propeller cavitation noise limited the range to 200–250 m when the ship traveled faster than 7 kt. Typically, the *Vickers* was underway once or twice a day, repositioning to the anticipated updrift edge of the watch circle.

Ship position and velocity were determined with a Magnivox CA code GPS receiver. The GPS-derived ship's velocity estimates had an associated noise variance approximately a factor of 10 greater than sonar-derived relative velocity errors. To reduce the signature of this noise, it was necessary to filter the GPS data without smoothing or distorting the sharp crests of the observed waves. Typical low-pass filters would broaden the soliton waveform significantly. To minimize broadening, the ship's velocity record associated with each soliton crest was approximated by the analytic form $u = A\ \mathrm{sech}^2[(x - ct)/L]$. This analytic signal was then subtracted from the GPS velocity record, removing the gross signature of the crest. Twelve-hour segments of the residual field were fitted with a fifth-order polynomial (Jan) or filtered with a fifth-order Butterworth low-pass filter (5 cph cutoff, Feb). The model velocity pulses were then recombined with the filtered ''background velocities'' to produce a final estimate of absolute ship's velocity.[1]

## 4. A brief review of dynamics

Korteweg and de Vries (1895) explored the propagation of weakly nonlinear gravity waves of horizontal scale long compared to the water depth. They derived the now famous ''KdV'' equation

$$\frac{\partial \eta}{\partial t} + c' \frac{\partial \eta}{\partial x} + \alpha \eta \frac{\partial \eta}{\partial x} + \beta \frac{\partial^3 \eta}{\partial x^3} = 0, \qquad (1)$$

where $c'$ is the phase speed of an infinitessimal wave,

[1] In applying this technique, there is no assertion that the solitons in fact have a $\mathrm{sech}^2$ waveform. As long as the difference between the actual waveform and the $\mathrm{sech}^2$ profile occurs at sufficiently large scale that it is fit by the polynomial or passed by the filter, the undistorted waveform will be recovered.

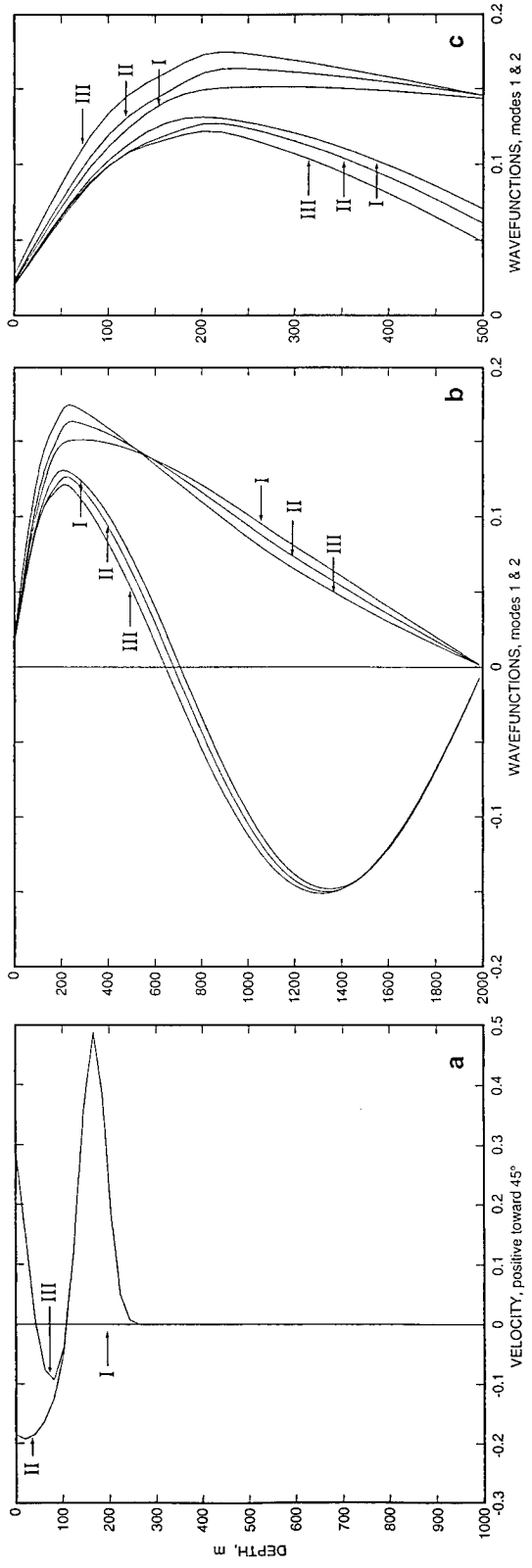


FIG. 4. Theoretical solutions $\phi_1$, $\phi_2$ to the Taylor–Goldstein equation for the idealized cases of I—no current, II—an undercurrent and South Equatorial surface current, III—an eastward surface flow. (a) The current structure, and (b) full ocean depth and (c) upper-ocean close-ups of the modal functions.

and $\alpha$ and $\beta$ are the coefficients of nonlinearity and dispersion. They identified solutions of the form

$$\eta = \eta_0 \operatorname{sech}^2[(x - ct)/L]. \tag{2}$$

This particular waveform is a solution provided the propagation speed $c$ and length scale $L$ assume values determined by $\eta_0$, $\alpha$, and $\beta$ such that nonlinear and dispersive tendencies exactly cancel.

The KdV equation has been extended to two-layer fluids in the limit that the horizontal scale is long compared to the depth of either layer. Subsequent extensions have treated the case of a lower layer comparable to $L$ or greater (Davis and Acrivos 1967; Ono 1976) and to an infinitely deep lower layer (Joseph 1977). All of these second-order solutions have the property that propagation speed increases and horizontal scale decreases with increasing wave amplitude.

The problem has been generalized to the case of continuously stratified fluids with background shear (e.g., Lee and Beardsley 1974). Here solutions take the form

$$\psi(x, z, t) = \sum_n a_n \phi_n(z) F_n(x - c_n t), \tag{3}$$

where $\psi$ is the streamfunction of the flow and the $\phi_n$ are eigenfunctions of the Taylor–Goldstein equation, which for two-dimensional, nonrotating flow takes the form

$$\phi_{zz} + \left[\frac{N^2 - \sigma^2}{(c' - U)^2} + \frac{U_{zz}}{(c' - U)}\right]\phi = 0$$
$$\phi = 0 \quad \text{at } z = 0, -H \tag{4}$$

(e.g., Thorpe 1969). Solutions for modes one and two are presented in Figs. 4b,c. The cases of no mean current, an idealized South Equatorial Current and Undercurrent, and a three-layer flow, with the eastward surface current corresponding to late December (Fig. 4a) are considered. The effect of these currents on the northeastward propagation of low mode waves is minor. Slight changes in modal shape are detectable. Differences in dispersion are seen at high wavenumbers, where the Undercurrent advects slowly propagating waves toward the east.

The coefficients of nonlinearity, $\alpha$, and dispersion, $\beta$, are given in terms of the modal solutions, $\phi_n$, as well as $N^2$ and $U$. For a Boussinesq fluid in the absence of mean currents, the relevant expressions simplify to

$$\alpha = \left(\frac{3}{2}\right)c_n' \int_{-H}^{0} (\phi_n')^3 \, dz \Big/ \int_{-H}^{0} (\phi_n')^2 \, dz \tag{5}$$

$$\beta = \left(\frac{c_n'}{2}\right) \int_{-H}^{0} \phi_n^2 \, dz \Big/ \int_{-H}^{0} (\phi_n')^2 \, dz \tag{6}$$

(Ostrovski and Stepanyants 1989). For the *Vickers* site, $c_1' = 2.4$ m s$^{-1}$, $\alpha = -0.025$ s$^{-1}$, and $\beta = 2.4 \times 10^5$ m$^3$ s$^{-1}$, under the normalization $(1/H)\int_{-H}^{0}\phi^2 dz = 1$. Ostrovski and Stepanyants (1989) review numerous de-

velopments of the theory, with a focus on oceanic solitary waves.

With the advent of computers it was found that a rather arbitrary initial disturbance evolves into a ''train'' of ''solitary'' waves as it collapses and expands laterally. Liu et al. (1985) present numerical results that simulate the observed evolution of soliton trains in the Sulu Sea (Apel et al. 1985). Liu notes that the energy required for soliton growth is extracted from the decreasing potential energy of the initial disturbance, which trails behind the solitary wave train. Henyey and Hoering (1997) emphasize the intimate connection between the leading crests and the trailing ''aftermath.''

Borelike behavior is seen in the COARE observations (Henyey and Hoering 1997). However, the actual energetics are quite complex. In addition to the apparent extraction of energy from the underlying tide (Gerkema and Zimmerman 1995), the passage of soliton packets frequently triggers smaller-scale wave generation and dissipative events on preexisting subtidal shear layers. The observations suggest that the energy of these small-scale events is extracted from the subtidal background. Examples will be presented below.

Recently, Stanton and Ostrovski (1998) have presented shallow water observations where solitary waves exhibit the tendency to broaden (increase in scale) rather than narrow as amplitude is increased. They suggest that their waves are sufficiently energetic that the assumption of weak nonlinearity is no longer justified. Their observations are well matched by solutions to the third-order ''comb KdV'' equation:

$$\frac{\partial \eta}{\partial t} + (c' + \alpha\eta + \alpha_1\eta^2)\frac{\partial \eta}{\partial x} + \beta\frac{\partial^3 \eta}{\partial x^3} = 0, \quad (7)$$

with solutions of the form

$$\eta = \eta_0\{\tanh[(x - ct)/L + \delta] - \tanh[(x - ct)/L - \delta]\}. \quad (8)$$

Here $c$, $L$, and $\delta$ depend on background environmental parameters as well as wave amplitude (Lee and Beardsley 1974).[2] Using Stanton and Ostrovski's relations for a two-layer fluid, with $c = 2.4$ m s$^{-1}$, ocean depth $H = 2000$ m and upper-layer depth $h = 200$ m, we find $\alpha = -0.016$ s$^{-1}$, $\alpha_1 = -3.8 \times 10^{-5}$ (ms)$^{-1}$, and $\beta = 1.4 \times 10^5$ m$^3$ s$^{-1}$ for the COARE site.

Lamb (1997) has studied higher-order solitons numerically. He confirms the tendency of crests to broaden with increasing amplitude and notes the significant increase in mass transport associated with broader crests.

[2] Henyey and Hoering (1997) caution that at third order, terms that govern the interaction of the soliton with its environment must be considered as well.

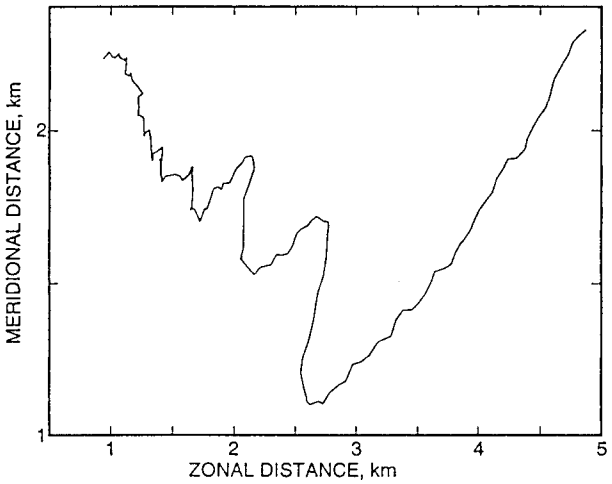


FIG. 5. Drift track of the R.V. *Vickers* over the 5-h period 850–1350 UTC 11 Jan 1993, during passage of a nonlinear wave train. The ship is initially at the upper right, drifting southwestward.

## 5. Event passage

Internal solitary waves were observed in COARE in conjunction with the spring tides of late November 1992, early January and early February 1993. The initial observation consisted of a single crest (40-m vertical displacement), which passed under the *Vickers* at 1400 UTC 28 November. Six groups of waves (consisting of 2, 2, 2, 3, 3, and 2 distinct crests) were seen between 9 and 12 January, with an additional seven groups (1, 2, 2, 2, 3, 3, and 1 crests) following between 7 and 12 February. The third crest, when seen, was often quite small and difficult to distinguish from the background. The underlying baroclinic tide appeared strongly nonsinusoidal over the few cycles preceding and following solitary wave sightings.

The most consistent indicator of solitary wave activity was the ship's navigation record. The record for 11 January (Fig. 5) shows the *Vickers*' initial southwestward drift interrupted by a series of three abrupt offsets toward the north-northeast, each corresponding to the passage of a soliton crest. The aggregate displacement of the ship (as well as local surface drifters, biota, and the upper ocean itself) exceeded 1.5 km. Following passage of the packet, the southward component of drift is reversed while the westward component remained, resulting in the observed net flow to the northwest.

Given its propensity to ''surf,'' the ship spends proportionally longer time in the soliton crests than would a true Eulerian observer. To compare observed waveforms with theoretical models it is necessary to account for this advection. Henceforth, as a convention, observations presented as a function of time are given in the ship's (distorted) reference frame. Observation presented as a function of distance are corrected for the advection of the ship.

To account for distortion, it is necessary to determine

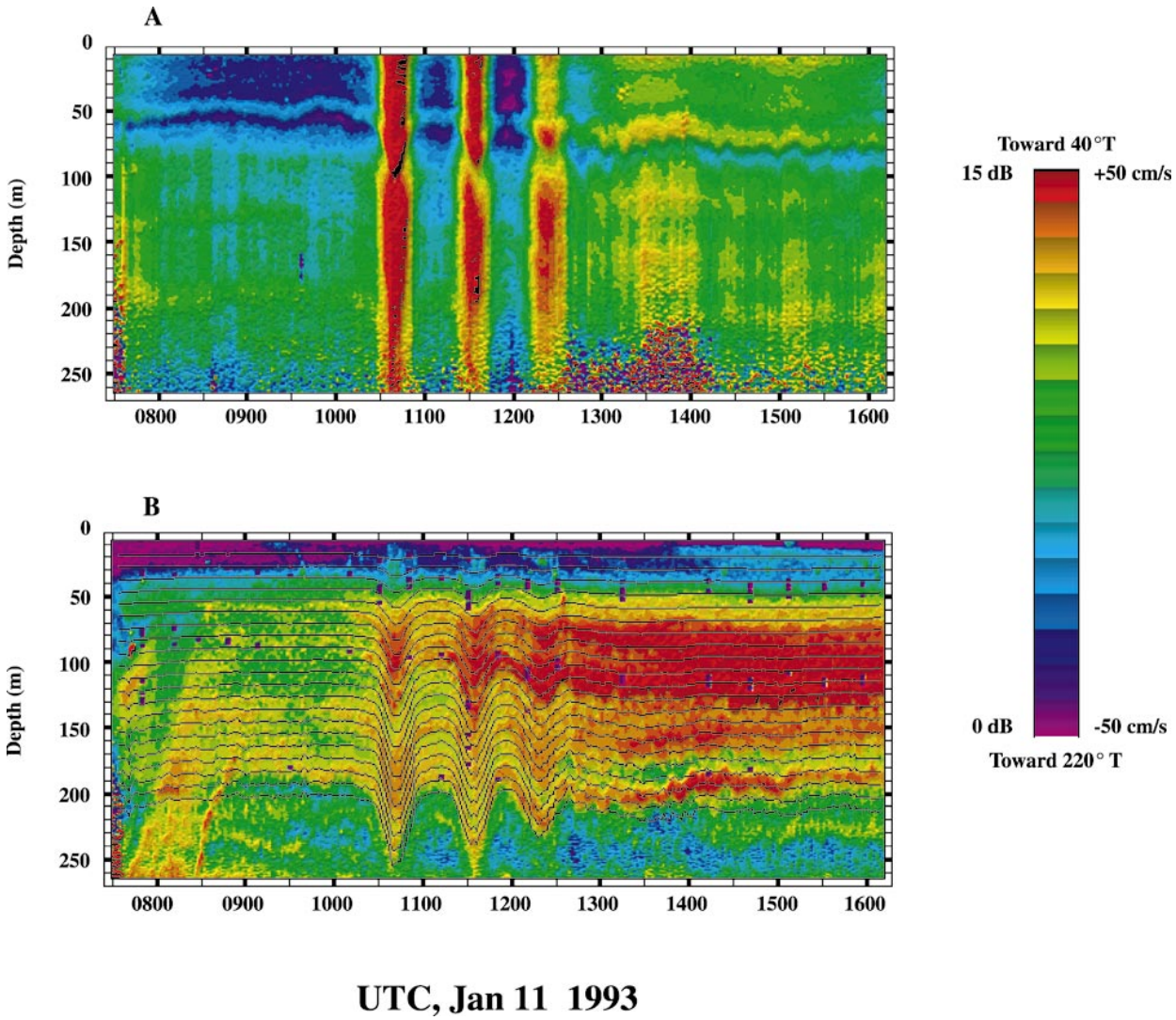


FIG. 6. (a) The along-path (40°–220°) component of absolute ocean velocity for the 1030 UTC 11 Jan event. Sonar precision degrades below 200 m, a consequence of low signal level at great range. The fine vertical stripes are the signature of the GPS error, which remains after the filtering techniques described in the text have been applied. (b) The acoustic scattering strength field at 161 KHz, following adjustment for inverse square spreading and attenuation. Colors represent variation on a logarithmic scale over a factor of thirty. Calculated flow streamlines are superscribed in black. Regions of the thermocline with unstable density gradient, as determined by the CTD, are indicated by purple rectangles.

the propagation direction of the wave packets. This process is complicated by the intensity of the ''background'' equatorial currents. The strong time variability of the underlying baroclinic tide and the borelike aftermath of packet passage, both of which are phase locked to the packets, also pose a problem. Estimated propagation directions vary between 25° and 50°T, with most packets heading between 35° and 45°T.

It is convenient to present observations in a coordinate frame rotated in the direction of wave propagation. To standardize, along-path (longitudinal, toward 45°T) and transverse (toward 135°T) coordinates are used for all observations, as well as for the spatial reconstructions necessary to correct for advective distortion.

The 1000–1300 UTC 11 January packet is presented as representative of the COARE solitons. The component of ocean velocity in the direction of soliton travel is given in Fig. 6a. The velocity is given relative to the earth, but in the advected reference frame of the ship, as displaced by the passing waves. The distortion resulting from this advection is of order $u/c$, which reaches peak values of ~0.3 during crest passage, but is usually much smaller.

The three wave crests appear ordered in amplitude. The largest has a horizontal velocity that exceeds 0.8 m $s^{-1}$ relative to the earth and 1.0 m $s^{-1}$ relative to the background mixed layer. The crests are spaced by ~50 min. Had the ship remained at a fixed position, the in-

terval between crests would be reduced by approximately 10 min.

The packet passage occurs several hours after the internal tidal elevation of the thermocline reaches maximum (around 0800 UTC, as determined by the vertical displacement of the horizontal velocity field). Surface layer (0–80 m) currents continue toward the southwest for several hours following the first soliton, transitioning to a northwest flow only after passage of the third. This borelike behavior is reminiscent of observations of Osborne and Burch (1980, their Fig. 8). In COARE, the asymmetry of the tide is most pronounced in the surface layer, less so at depth.

The streamfunction, $\psi$, of the flow, where $\partial\psi/\partial z = c - u$, $\partial\psi/\partial x = w$, can be inferred directly from the observations, under the assumption that $\partial/\partial x = c^{-1}\partial/\partial t$. The phase speed $c$, here set at 2.4 m s$^{-1}$, is a free parameter. For $c \gg u$, results are not sensitive to its assumed value. Inferred streamlines, contours of constant $\psi$, are given in Fig. 6b. Jitter in the vertical displacement of the deep streamlines is a consequence of GPS noise.

The intensity record (Fig. 6b) shows the arrival of the zooplankton migration at local dusk, 0800 UTC. From 0900 through 1020 the existing scattering field evolves but little. The solitons are seen to depress the scattering layers. Observed vertical displacements are in good agreement with the calculated streamlines. Correspondence degrades following the third crest. Apparently, the assumption of nondispersive 2D flow required in the streamline calculation is not justified in this region.

Acoustic scattering strength increases in the core of the first soliton, decreases following its passage, and then increases with the passage of each subsequent crest. Scattering levels remain high for more than four hours following the last crest in the packet. Evidence of increased scattering is present in all COARE soliton observations, both day and night.

Bragg scattering from microscale ($\lambda_B = 0.5\lambda_{\text{sound}} = 0.46$ cm) fluctuations in the sound speed field is responsible for the increased acoustic return (Thorpe and Brubaker 1983; Goodman 1990; Seim and Gregg 1995). The increased structure in the associated temperature and salinity fields is a consequence of local turbulent events that follow passage of the solitons. This interpretation is supported by comparison with the mixed layer, where there is relatively uniform scattering. In such an isothermal, isohaline region, turbulent motion does not produce the finescale sound speed fluctuations required for increased Bragg scattering (Thorpe and Brubaker 1983).

The ''turbulence'' fails to decay in the hours following soliton passage. We note that salinity structures at the Bragg scale can be responsible for much of the scattering increase (Seim and Gregg 1995). A characteristic diffusive decay time for salinity structure is of order $\lambda_B^2/\nu_s \approx 4$ h, where $\lambda_B$ is the Bragg length scale, and $\nu_s$ is the molecular diffusivity of salt.[3] Long after active turbulence ceases, elevated scattering levels persist. The salinity fine structure acts as a nearly passive tracer, providing an ''acoustic dye'' that marks the advective stirring following event passage. The time evolution of this ''dye'' reflects not only the local generation and decay of fine structure, but lateral advection as well. Detailed interpretation is thus rendered difficult.

Profiles of density, temperature, and salinity have been obtained at 12 min intervals to a depth of 180 m throughout the passage of the January solitons. The purple rectangles in Fig. 6b represent regions where unstable density gradients are encountered. The gradient is here determined as a 5-m first difference. Persistent overturning is seen at the base of the surface layer (45–60 m) and in a layer centered at 110 m. The overturning in these layers precedes the arrival of the solitons, emphasizing the marginal dynamic stability (Miles 1963) of the equatorial currents. The 1130 UTC profile coincides with the passage of the second crest. Multiple overturns are observed between 120 and 180 m, as well as in the weakly stratified layer.

The transverse velocity as well as longitudinal and transverse components of shear are presented in Fig. 7. Near-surface velocities (a) show an ~0–10 cm s$^{-1}$ northwestward flow, unaffected by soliton passage. The undercurrent is seen flowing to the southeast between 120 and 200 m. Strong shears (Figs. 7b,c) are established in the weakly stratified region 40–90 m, as well as within and below the undercurrent. The vertical advection of these features mimics that of the flow streamlines and the acoustic scattering field. The intrinsic shear of the nonlinear waves is difficult to distinguish against this background (see Fig. 12). Similarly, there is no obvious interaction between the solitons and the equatorial background, in spite of the fact that the undercurrent is vertically advected $\pm 50$ m in a half-hour, assuming horizontal slopes approaching 1:20 in the process.

To quantify the distortion in Figs. 6 and 7 associated with the advection of the ship, the average near-surface (10–40 m) velocity of the 1000–1300 UTC 11 January event (a borelike example) is presented in terms of equivalent along-path range (Fig. 8). Here it is assumed that the solitons propagate northeastward at $c = 2.4$ m s$^{-1}$. The true crest shapes are noticeably steeper than those observed in the advected reference frame of the ship. Analytic solutions of Joseph's (1977) equation are steeper yet, when coefficients of nonlinearity and dispersion appropriate to the COARE site are applied. Cubic soliton solutions [Ostrovski and Stepanyants 1989, Eq. 7a] fit the true velocity profiles substantially better.

[3] The diffusivity of heat is approximately two orders of magnitude greater than that of salt, leading to a decay time of several minutes at the Bragg scale.

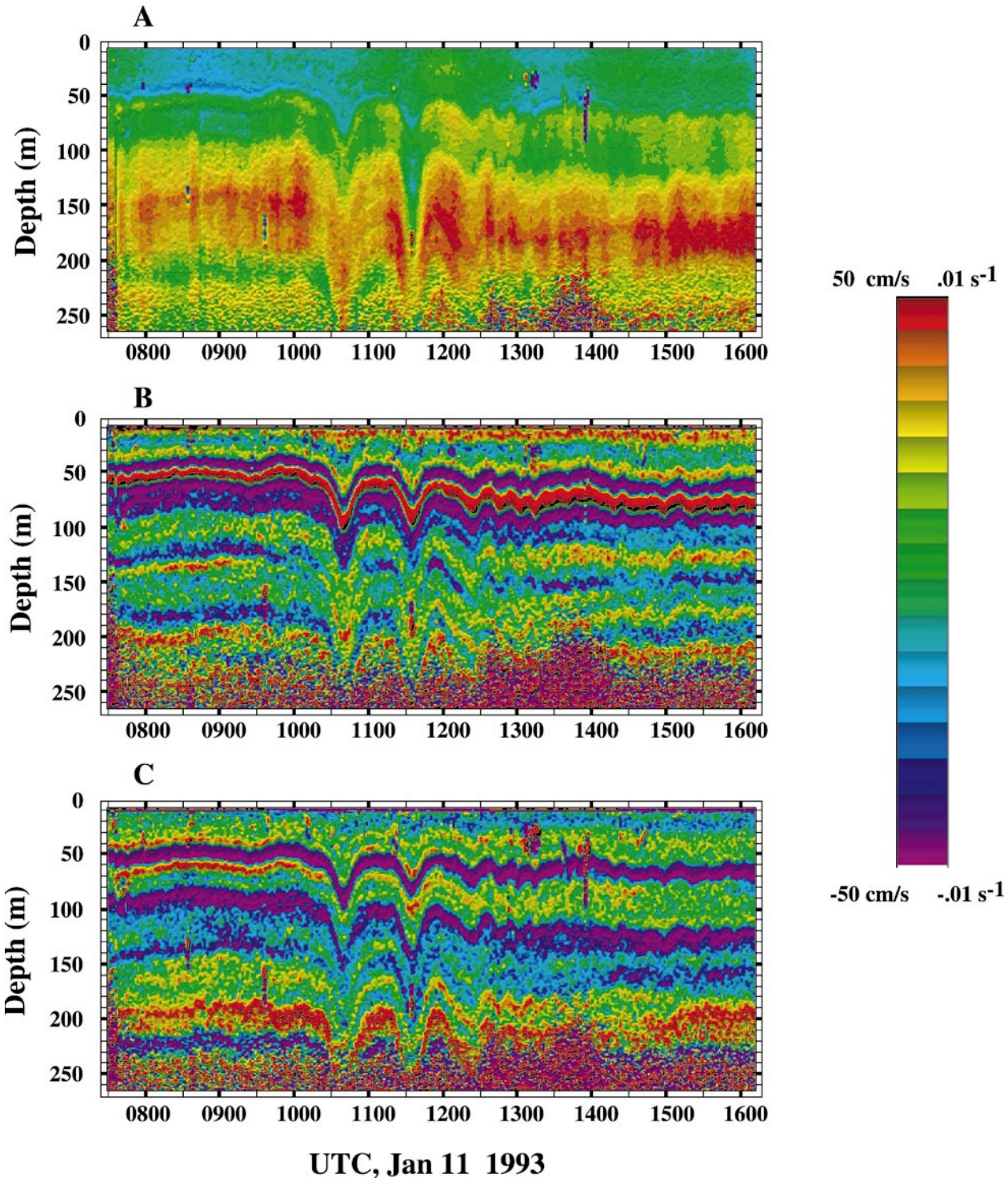


FIG. 7. (a) The transverse component of flow velocity for the 11 Jan event. Positive velocities are toward 130°. Rectangular scars in the record correspond to acoustic reflections from the profiling CTD, which is occasionally advected into one of the sonar beams by the strong currents. (b) Longitudinal and (c) transverse shears are taken as a 5-m vertical difference of the velocity data.

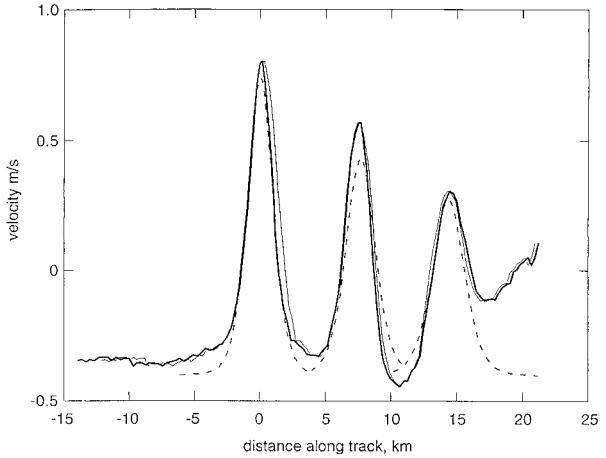


FIG. 8. The longitudinal component of soliton current (10–40 m average) presented as a function of along-track range (dark line) and as observed (light line) in the advected reference frame of the ship. Advection broadens the width of the first arrival significantly. The effect diminishes with subsequent arrivals. Fits of a cubic soliton (dashed line) are shown for coefficients $\alpha = -0.016$, $\alpha_1 = -3.8 \times 10^{-5}$, and $\beta = 1.4 \times 10^5$, which are appropriate to the site. An effective upper-layer depth of $h = 200$ m is assumed in this calculation.

Stanton and Ostrovski (1998) found this to be the case for shallow water solitons as well.

## 6. Sea surface displacement and perturbation pressure

With knowledge of the absolute fluid velocity, one can infer the sea surface elevation associated with soliton passage, $\eta_0$, directly from Newton's second law, that is,

$$\frac{Du}{Dt} = -g\nabla_h\eta_0. \tag{9}$$

The surface elevation comes from the integral of $\nabla_h\eta_0$ under the assumptions that the motion is 2D, of unchanging form, and nondissipative. Moving at the phase speed of the wave:

$$\frac{Du}{Dt} \cong (u - c)\frac{\partial u}{\partial x} = \frac{\partial}{\partial x}\frac{(u - c)^2}{2} = -g\frac{\partial \eta_0}{\partial x}. \tag{10}$$

Integrating with respect to $x$,

$$\eta_0 \approx -(u - c)^2/2 = p_0/\rho g, \tag{11}$$

where $p_0$ is the pressure at $z = 0$, the position of the undisturbed sea surface. This expression becomes exact in the hydrostatic limit.

The nonhydrostatic equivalent is Bernoulli's equation, which states that streamwise changes to flow kinetic energy are associated with perturbation pressures, $p'$, which do work on the (incompressible) fluid:

$$\frac{D}{Dt}\left\{\frac{\rho[(u - c)^2 + w^2]}{2} + p'\right\} = 0. \tag{12}$$

Knowing the flow streamfunction $\Psi$, the total kinetic energy $\rho[(u - c)^2 + w^2]/2$ can be calculated as a function of stream coordinates and distance along the soliton track. The associated perturbation pressure for the 11 January soliton is presented in Figs. 9 and 10. The (hydrostatic) equivalent sea surface displacement $\eta' = p'/\rho g$ is used to represent the pressure under the assumption that the total pressure, $P = p' + \rho gz$, vanishes at the sea surface. It is seen that the sea surface elevations associated with crest passage exceed 0.2 m. Maximum sea surface slopes of order $10^{-3}$ are implied. These values compare closely with estimates of dynamic height calculated from density field measurements (Picaut et al. 1995; Pinkel et al. 1997).

For the initial three crests, the depth variability of the perturbation pressure is suggestive of a mode-one internal waveform. The trailing ''bore,'' in contrast, is largely confined to the mixed layer. This difference in vertical dependence is emphasized in Fig. 10. Clearly, as ''solibore'' models are extended from two-layer (Henyey and Hoering 1997) to continuously stratified fluids, the matter of depth dependence will require careful attention.

## 7. Energetics and generation

In Figs. 11a,b profiles of kinetic energy for the six January events and the seven February events are presented. These are based on depth–time records of longitudinal velocity. The task is complicated by the presence of background currents that, in the case of the tide, appear in fixed phase with the solitons. Energy density is computed relative to two candidate backgrounds. Taking a 20-min average velocity just prior to soliton arrival as the background, relatively large energy densities, $\sim$0.075 MJ m$^{-2}$, are seen (Figs. 11a,b blue line). If a 6-h average longitudinal velocity is taken for the background, smaller apparent energy densities, $<$0.05 MJ m$^{-2}$, result. The ''short advance'' averages typically show upper-ocean flow toward the oncoming crest. The difference between the absolute velocity and this background is larger than the absolute velocity alone. In contrast, when a 6-h mean velocity is considered, fluctuations about this background appear much smaller. The energy density of the secondary arrivals is particularly sensitive to choice of background.

As a second complication, accurate estimates of absolute velocity are available in only the top 10% of the water column. Using the theoretical mode-one vertical wave functions (Figs. 4b,c), it can be shown that 80% of the kinetic energy in the waveguide occurs in the upper 170 m. [Similarly, using the wave functions and the observed profile of $N^2$, we find 75% of the potential energy in the water column is found in the top 170 m.] Observed energy levels are adjusted so as to represent the entire water column (Fig. 11, Table 1).

It is common to characterize waves in terms of energy per meter of crest. Here the task is complicated in that

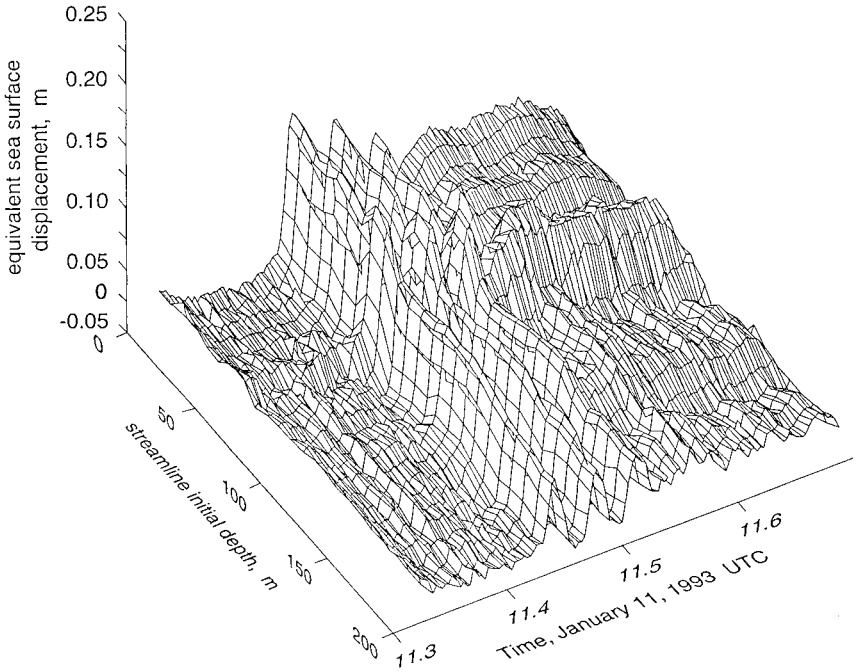


FIG. 9. Deformed surface representation of perturbation pressure for the 11 Jan event, as estimated from Bernoulli's equation. Data are displayed in terms of equivalent hydrostatic sea surface displacement $\eta' = p'/\rho g$ and are presented in stream coordinates. The ordinate gives the initial depth of each reference streamline. Sea surface displacements of order 0.25 m are inferred.

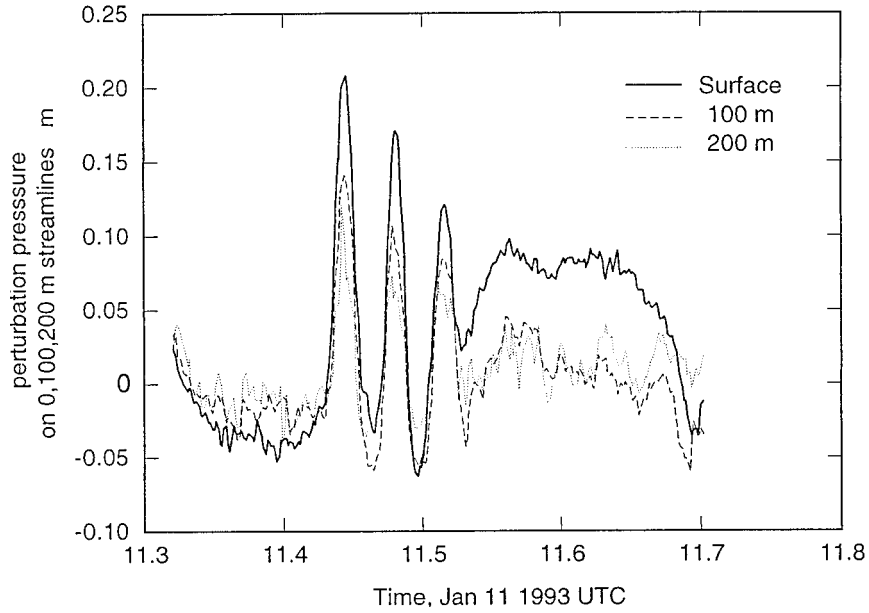


FIG. 10. Records of perturbation pressure along streamlines whose initial depths are 0, 100, and 200 m, illustrating the differing depth dependencies of the solitons and the borelike aftermath. Pressure is presented in terms of equivalent sea surface displacement.

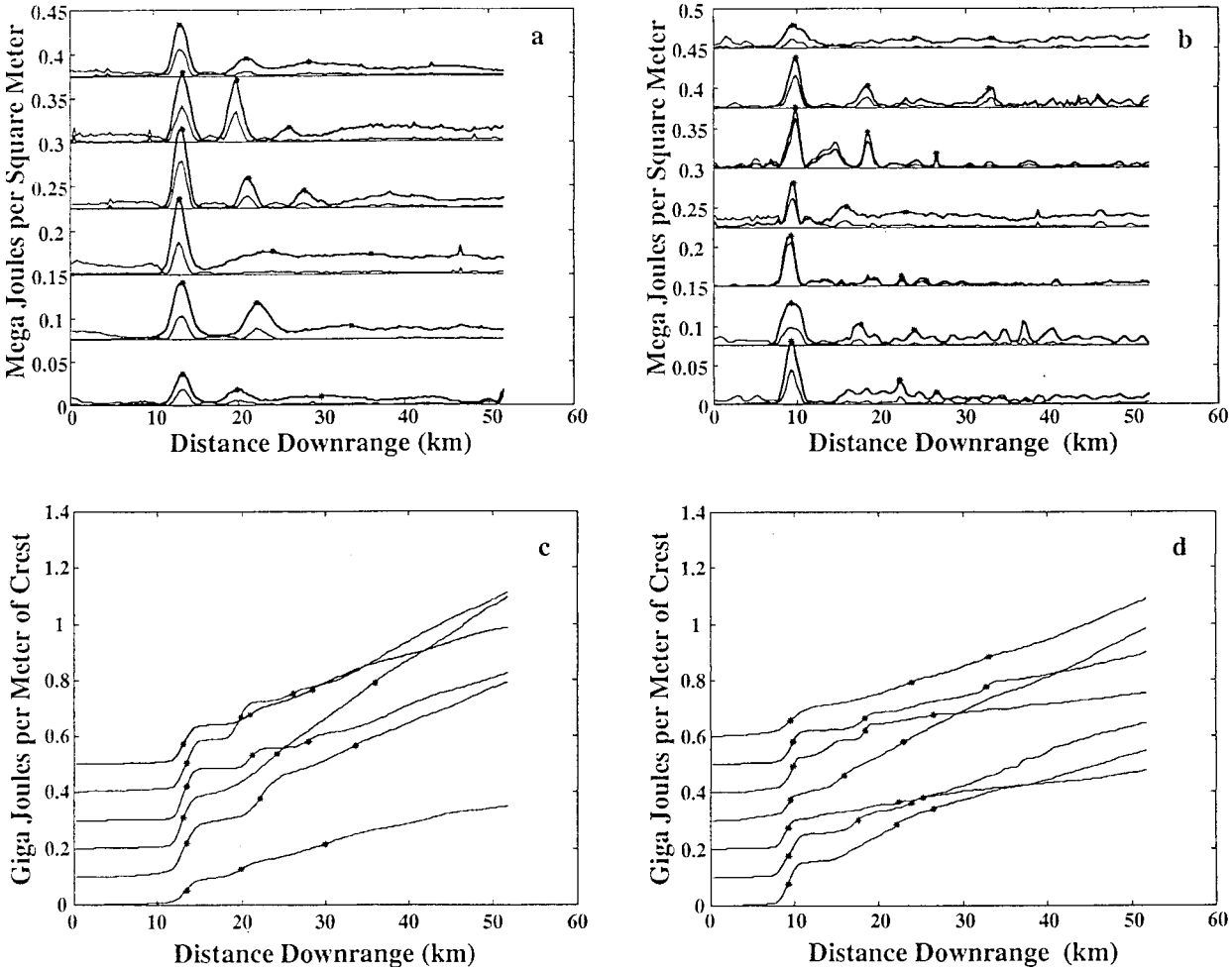


FIG. 11. Kinetic energy density for the (a) Jan and (b) Feb solitons. The first event of each month is presented as the bottom pair of curves. Subsequent events are offset by 0.075 mJ $m^{-3}$. The upper curves in each pair are associated with velocities relative to a background flow determined as a 20-min average prior to the arrival of the first crest. Lower curves give energy densities from velocity relative to a 6-h average, spanning the event arrival. Values are determined from an integration over the upper 170 m, which is augmented by the factor 1.25 to account for contributions from greater depths. Kinetic energy per meter of crest, for the (c) Jan and (d) Feb events, determined as a running integral of the data in a,b. Estimates are based on velocity relative to a 20-min average taken before the arrival of the first crest.

TABLE 1. The time, latitude, and longitude at which the initial crest in each packet is encountered. Peak kinetic and potential (January) energy densities for the crests, in units of $10^6$ J $m^{-2}$, and the observed time interval between crests are also presented. Values are not given if soliton velocities could not be well separated from the background flows.

| Packet | Yearday 1993 (UTC) | South latitude | East longitude | $KE_1$ | $PE_1$ | $\Delta t_{12}$ (min) | $KE_2$ | $PE_2$ | $\Delta t_{23}$ (min) | $KE_3$ | $PE_3$ |
|---|---|---|---|---|---|---|---|---|---|---|---|
| Jan A | 9.9465 | 1.9940 | 156.2456 | .0354 | .020 | 44 | .0180 | .016 | | | |
| Jan B | 10.4326 | 2.0367 | 156.2028 | .0654 | .0198 | 60 | .0429 | .017 | | | |
| Jan C | 10.8894 | 2.0738 | 156.1723 | .0864 | .0188 | | | | | | |
| Jan D | 11.4422 | 2.0758 | 156.3042 | .0911 | .019 | 54 | .0347 | .0136 | 46 | .020 | .011 |
| Jan E | 11.9560 | 2.0769 | 156.3313 | .0794 | .019 | 44 | .0704 | .0184 | 44 | .017 | .011 |
| Jan F | 12.4309 | 2.1024 | 156.2208 | .0579 | .0198 | 54 | .0205 | .0122 | 52 | .0161 | .011 |
| Feb A | 38.8129 | 2.1391 | 156.3368 | .081 | | | | | | | |
| Feb B | 39.3253 | 2.0502 | 156.2236 | .054 | | 58 | .027 | | | | |
| Feb C | 39.8781 | 2.0405 | 156.3330 | .065 | | | | | | | |
| Feb D | 40.8835 | 2.0259 | 156.0519 | .056 | | 44 | .026 | | | | |
| Feb E | 41.3932 | 2.0704 | 156.1475 | .077 | | 60 | .045 | | | | |
| Feb F | 42.4722 | 2.1027 | 156.3279 | .036 | | 60 | .027 | | | | |
| Feb G | 43.0166 | 2.0294 | 156.1810 | .030 | | | | | | | |

there is no uniquely definable wavelength over which to integrate the known energy per area. This difficulty can be side-stepped by presenting the energy per meter as a running integral of energy per area, with the integration taken along the propagation path (Figs. 11c,d). The soliton crests appear as regions of high slope. A 20-min average velocity background, taken just prior to the arrival of the initial crest, is subtracted from the longitudinal velocity prior to forming the energy estimates. In cases where the background flow evolved significantly following soliton passage, the energy per meter continues to rise with increasing distance.

Potential energy can be estimated for the January events, when a CTD was profiling to 150 m at 12-min intervals. The 12-min measurements of $N^2$ were interpolated to 2-min spacing along a set of specified streamlines. Using the vertical displacement of the streamlines as a surrogate for the vertical displacement of isopycnals, a potential energy estimate is obtained (Table 1). While the contribution to potential energy from the sea surface vertical displacement has not been considered here, it can be shown to be small (Pinkel et al. 1997). Kinetic energy exceeds potential energy by a factor of 2–5 in the January solitons.

In considering the generation of these waves it is of value to revisit the larger-scale energetics of the region. Egbert's (1997) value of 90 GW for $M_2$ dissipation in his Region 6 (an elongate stretch of the central-western equatorial Pacific) corresponds to an average rate of approximately 0.003 W m$^{-2}$. Over a 12-h tidal cycle roughly 130 J m$^{-2}$ are being extracted from the barotropic tide in the region. A 0.2 GJ m$^{-1}$ solitary wave packet represents the energy lost by the tide over a 1500-km stretch of ocean, concentrated in 1–10 km.

Turning attention to the baroclinic tide, the rms tidal band (1/15–1/10 cph) currents averaged over the upper $H = 170$ m are 0.083 m s$^{-1}$, 0.070 m s$^{-1}$, and 0.080 m s$^{-1}$ for the November–December, December–January, and January–February legs of the *Vickers* cruise. When modeled semidiurnal barotropic currents of F98 (their Table 3.1) are removed, values of 0.075 m s$^{-1}$, 0.058 m s$^{-1}$, and 0.069 m s$^{-1}$ remain. Considering only the upper 170 m, mean semidiurnal kinetic energy densities, $E_k = \frac{1}{2}\rho\langle u^2\rangle H$, of ~478, 285, and 404 J m$^{-2}$, and corresponding kinetic energy fluxes of $F_k = c_g E_k = 1147$, 684, and 971 W m$^{-1}$, are implied. Here we have assumed $c_g$, the group velocity, is equal to $c$, a good approximation for semidiurnal waves near the equator. Assuming potential energies comparable to kinetic, these fluxes (from the upper 170 m alone) are a factor of 2–4 greater than the F98 report for the COARE region as a whole. The F98 value is based on a single sinusoidal constituent that is phase locked to the astronomical forcing. It is thus not surprising that the total observed flux is greater. It is also likely that the *Vickers* site represents either a lateral flux convergence or a vertical convergence associated with the reflection from upper-ocean structure and the surface itself (Thorpe 1998).[4]

Even though the local semidiurnal baroclinic energy density is perhaps too large to be characteristic of the COARE domain, it is small compared to the energy density of the nonlinear waves. Typical solitary wave events have velocities 5–10 times the underlying tide, confined to a region $(1/5)^2$–$(1/10)^2$ of a tidal wavelength. Given that the vertical modal waveforms of the tide and the solitons are similar, the total kinetic energies (joules per meter of crest) are also comparable.

## 8. Soliton propagation

A surprising aspect of the COARE observations is the apparent ease with which the solitons propagate through the highly sheared equatorial environment. High-frequency internal waves are also known to displace the low-frequency shear field, without obvious interaction (Pinkel and Anderson 1997).

The independence of low and high frequency fields can be understood in terms of vorticity conservation, which, for a stratified incompressible fluid, can be written

$$\frac{D\overline{\zeta}}{Dt} = \overline{\zeta}\cdot\nabla u + \nu\nabla^2\overline{\zeta} + \nabla p \times \nabla\left(\frac{1}{\rho}\right) \qquad (13)$$

[Turner 1973, Eq. (1.35)]. The three terms on the right describe how stretching, dissipation, and baroclinicity modify the vorticity of a fluid parcel.

Consider the case of a soliton propagating in the $x$ direction through a loss-free, nonrotating ocean, with a background shear in the $x$–$z$ plane, $\zeta_y = \partial u/\partial z = O(10^{-2})$ s$^{-1}$. The $y$ component of the vorticity equation reduces to

$$\frac{D\zeta_y}{Dt} = \left[\nabla p \times \nabla\left(\frac{1}{\rho}\right)\right]_y = -N^2\left(\frac{\partial\eta}{\partial x} - \frac{1}{\rho g}\frac{\partial p}{\partial x}\right). \qquad (14)$$

Vorticity is produced when the slope of density surfaces, $\partial\eta/\partial x$, does not coincide with the slope of isobaric surfaces. Bounding the magnitude of the terms, $N^2 \le 10^{-4}$ s$^{-2}$ and $\partial\eta/\partial x < 0.1$. The value of $-(1/\rho)g\partial p/\partial x$ never exceeds the sea surface slope, of order $5 \times 10^{-3}$. Thus, $D\zeta_y/Dt \le 10^{-5}$ s$^{-2}$. A fluid parcel would have to experience these extreme conditions steadily for $10^3$ s $\approx$ 20 min before a change in vorticity occurred that is comparable to the background itself. Isopycnal slopes of order 0.1 are, in fact, experienced for just a few minutes. It's understandable that shears in the $x$–$z$ plane appear to be advected as if they are nearly passive.

The baroclinic term describes the creation of the vorticity intrinsic to the soliton itself. In contrast, the mag-

[4] Horizontal velocities double in the near field of a ray reflection: kinetic energy levels quadruple. However, the horizontal energy flux $F = \langle p'u'\rangle$ does not increase in the region of the reflection, as the pressure perturbation decreases.

nitude of the vortex stretching response, $\overline{\zeta} \cdot \nabla u$ is proportional to the preexisting vorticity. Here the role of the background is more interesting. Consider shear in the $y$–$z$ plane, orthgonal to the propagation path. Here $\zeta_x = \partial v/\partial z$ and

$$\frac{D\zeta_x}{Dt} = \zeta_x \frac{\partial u}{\partial x}. \tag{15}$$

A characteristic $e$-folding time for the background transverse shear is $|(\partial u/\partial x)^{-1}| = 100$ s (peak) to 1000 s (average). The longitudinal convergence associated with soliton arrival might perturb the background noticeably. In the COARE data, this effect is not obvious (Fig. 7c), given the gross vertical advection of the shear field.

Is this a mechanism capable of inducing small-scale instability? In the upper ocean, soliton arrival is accompanied by vortex compression ($\partial u/\partial x < 0$), which serves to reduce cross-track shear magnitude. With passage of the crest the resulting vortex stretching restores the transverse shear to original levels. However, there is a zero crossing in the vertical profile of horizontal velocity and at great depth, the sign of $\partial u/\partial x$ reverses. Small increases in transverse shear can be expected as solitons pass.

## 9. Soliton dissipation

The typical amplitude of the largest deep sea solitons is 80–100 m. Amplitudes greater than 100 m are rarely reported [e.g., see Bole et al. (1994), who present observations in the South China Sea.] Does some instability process limit soliton amplitude? Energy exchange with the underlying tide, as well as loss to the trailing bore (Henyey and Hoering 1997), to trailing internal waves, and directly to turbulence, must be considered.

Bogucki and Garrett (1993) examined the threshold imposed by energy losses directly to turbulence. They consider an essentially two-layer fluid. Soliton shear is concentrated in a thin but finite transition region that separates the upper and lower layers. The maximum amplitude of a stable soliton is established by the Richardson number in this transition region.

In the continuously stratified western Pacific, the shear in a mode-one soliton is broadly distributed with depth. Given the ambient stratification, are the observed waves self-unstable to Kelvin–Helmholtz instability? With knowledge of the flow streamlines, the soliton can be effectively isolated from its background[5]: The Richardson number associated with the soliton itself can be estimated and compared with that observed from the total flow.

It is convenient to conduct this comparison in stream coordinates and consider the inverse Richardson number

$$R^{-1}(\psi, t) = \frac{s^2(\psi, t)}{N^2(\psi, t)} = \frac{s^2(\psi, t)}{\overline{N^2}(\psi)}\gamma(\psi, t). \tag{16}$$

Here $\overline{N^2}(\psi)$ is the preexisting background stratification, and

$$\gamma(\psi, t) = \frac{\partial \psi}{\partial z}\Big/\frac{\partial \psi_b}{\partial z} = \frac{(c - u)}{c} \tag{17}$$

is a strainlike quantity that takes on values greater than unity when streamlines are dilated relative to their background separation, less than unity when compressed.

The stability, shear, and Richardson fields are presented in Fig. 12. The strain, $\gamma$ (Fig. 12a), is essentially a normalized copy of Fig. 6a. Strains exceed 10% only in the crests of the first two solitons in the packet. Correspondingly, the background squared Väisälä frequency is only reduced by order 10% as the crests pass. The observed squared inverse Väisälä frequency $N^{-2}(\psi, t)$ is presented, in stream coordinates, in Fig. 12b. Data are obtained from CTD casts to 150 m, taken at 12-min intervals. Red regions indicate low buoyancy gradient. With the gross vertical displacement field ''removed,'' there is no apparent signature of soliton perturbation. The small variations observed are strongly affected by the coarse temporal sampling of the CTD.

In Fig. 12c, the intrinsic shear of the soliton train is estimated, using the time variation of a reference streamline (mean depth 150 m) and the depth dependence of a first-mode internal wave. The modal waveform is calculated through integration of the Taylor–Goldstein equation [Eq. (4)] using the actual buoyancy profile with a quiescent background assumed. The intrinsic squared shear peaks at $10^{-6}$ s$^{-2}$. Note that there is no sense of the self-advection of the shear by the soliton in this linear model.

In Fig. 12d, the observed squared shear is plotted in stream coordinates. Shears at the base of the mixed layers dominate the signal. Soliton passage is associated with slight changes in the magnitude and ''depth'' of the shear layers. The downward position jumps at 1040 and 1130 UTC indicate that the vertical displacement of the modeled streamlines is, in fact, less than the displacement of the shear layers. (The slow downward drift of the layers through the course of the record is also an indication of imperfection in the estimated streamfunction.) Note the difference in scales between Figs. 12c and 12d.

Figures 12e and 12f give the inverse Richardson field for a modeled weakly nonlinear soliton passing through the ambient buoyancy field (Eulerian frame) and the observed soliton (Fig. 12f is in stream coordinates, note different scales). In the model calculation the true mean Väisälä profile for the period is distorted by the modeled strain field (Fig. 12a) and combined with the modeled shear (Fig. 12c). The intrinsic soliton motion field is stable: Richardson numbers are a factor of 10 removed from critical values.

[5] The internal tide constitutes a significant fraction of the background. However, being low mode, it is associated with relatively little shear.

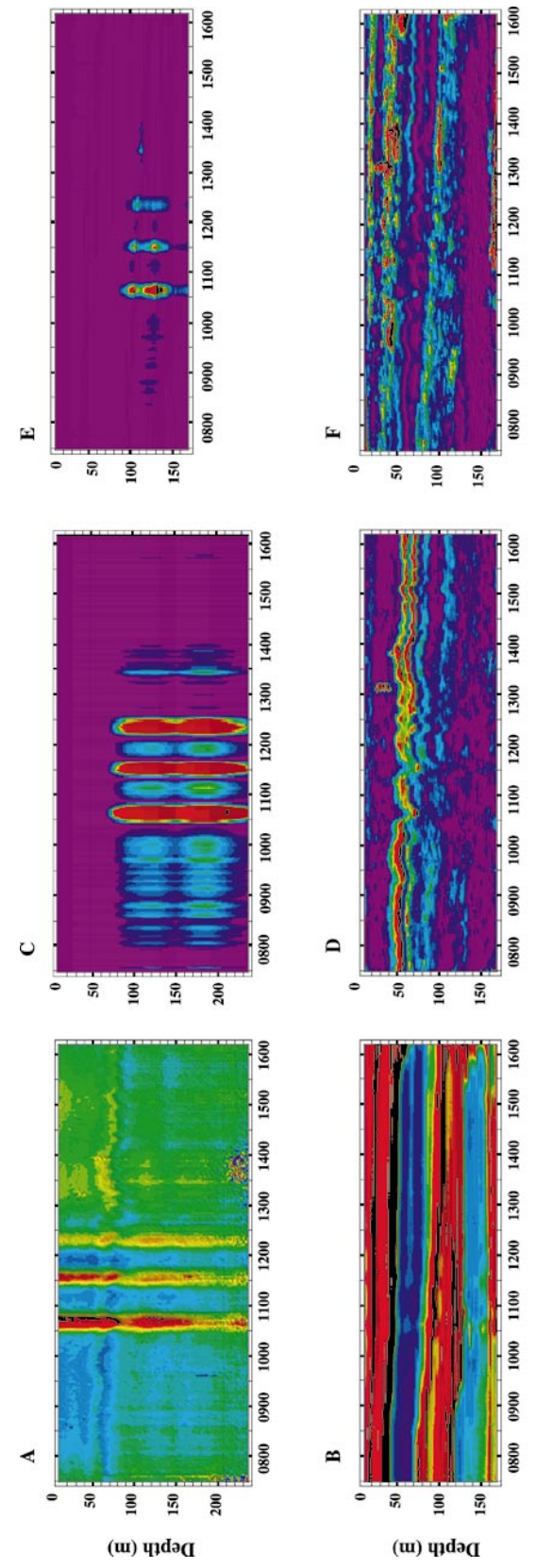


FIG. 12. Richardson number study. (a) The strain field associated with the passage of the 1030 UTC 11 Jan soliton. Positive strains, which approach 1.4, serve to reduce the background buoyancy frequency. (b) The observed inverse squared buoyancy frequency, $N^{-2}$, presented in stream coordinates. Regions of low stability are seen in red. The effect of soliton passage is barely perceptible. (c) The ''intrinsic squared shear'' of the event, obtained by fitting a theoretical mode-one horizontal velocity wave function (derived from Figs. 4b,c) to the observed velocity at 150 m, and then differentiating in depth. (d) Ambient squared shears, presented here in stream coordinates, are an order of magnitude greater than intrinsic. (e) Combining the background buoyancy profile with the intrinsic strain and shear, an intrinsic inverse Richardson number is obtained. Values are a factor of 10 removed from instability. (f) The observed inverse Richardson field in stream coordinates is not dramatically affected by soliton passage. However, local instabilities must be triggered, as evidenced by increases in acoustic scattering strength. Note that (a), (c), and (e) are Eulerian representations.

The estimate of the observed Richardson number field is formed using Väisälä values from the 12-min CTD profiles interpolated to 2-min intervals at fixed values of $\psi$ and merged with the 2-min shear data. The observed field indicates regions of low dynamic stability in the weakly stratified regions near the mixed layer base and around 100-m depth. The upper region is marginally unstable during the period immediately in advance of bore arrival when mixed layer waters are flowing toward the oncoming crests. It remains intermittently unstable through the record. Numerous overturns are detected by the CTD in this upper region. The deeper low-stability region becomes critical between 1300 and 1430 UTC. The CTD detects overturns (Fig. 6b) in this depth range, as well, starting at 1100 following passage of the first soliton.

Since overturns are occurring and the Richardson number is marginally critical in selected layers both before and long after the solitons have passed, one can presume that the energy dissipated here is not drained from the soliton itself. Given the observed increase in acoustic scattering strength (Fig. 6b), solitons are apparently effective in triggering instability on the background flow. In this sense, they represent a localized, time-dependent eddy diffusivity that acts on the near-equatorial flow field. However, the broad vertical spread of increased salinity fine structure (the ''red dye'' in Fig. 6b) is not accompanied by a corresponding vertical diffusion of the shear layers (Figs. 7b,c). The lateral (isopycnal) dispersion of water ''stirred'' at distant overturning sites creates the appearance of local vertical mixing.

## 10. Soliton tails and triggered disturbances

The final solitons of the February group were associated with distinct internal wave ''tails.'' Acoustic intensity and longitudinal and transverse velocity are presented for the events of 0800 UTC 10 February and 2330 UTC 12 February. The 10 February passage consists of two pronounced crests, the first perhaps exceeding 100 m in amplitude (Figs. 13a–c). A third crest, following closely after the second, is apparent at depths of 200 m but not near the surface. Shortly thereafter the upper thermocline breaks into oscillations of $\sim$5 m half-amplitude and 12-min period. The wavelike disturbances spread to 200-m depth in the 5 h after soliton passage and subsequently decay.

The soliton of 12–13 February, the last observed in COARE, consists of a single $\sim$50 m downward crest (Figs. 13d,f) followed almost immediately by an upper-ocean ($<$150 m) high-frequency response ($>$7.5 cph) and a lower frequency ($\sim$2 cph) response at very high mode. The high mode waves have a vertical half-wavelength of $\sim$80 m with amplitudes of $\sim\pm$20 m. The downward crests at depths below 150 m have significantly greater amplitude than the upward crests at $\sim$100 m. They appear extremely nonsinusoidal, with the upward displacement a mirror reflection of that downward. It is suggested that these high mode waves are interfacial solitons of the type investigated by Davis and Acrivos (1967). The COARE observations might represent a first sighting of these waves in the deep sea. [Qualification is necessary, in that we have no evidence that these motions are, in fact, of stable form.]

Akylas and Grimshaw (1992) have studied soliton wakes, motions generated by passing solitons, that drain energy from them. In the classical wake scenario, a high-mode soliton trails a sequence of short low-mode waves. The short wavelength wake is able to travel in fixed phase with (at the same speed as) the generating soliton by virtue of being of lower mode. However, the COARE solitons are first mode, themselves. Any short wavelength disturbance that they trigger necessarily propagates too slowly to keep up.

The energy associated with the COARE ''wakes'' is significant. Consider a soliton moving at $c = 2.5$ m s$^{-1}$ trailing a wake consisting of $\eta = 5$ m amplitude waves. If these occupy a 100-m vertical domain, H, the power required to create the wake is of order

$$\dot{E} = \frac{1}{2}\rho N^2 \eta^2 H c \quad [\text{W m}^{-1}]. \tag{18}$$

Using $N^2 = 4 \times 10^{-5}$ s$^{-2}$, $\dot{E}$ is of order 125 W m$^{-1}$, corresponding to a decay time for the soliton of order 10 days.

But is this energy coming from the soliton or the background shear? During the passage of these late-February solitons, a strong 30–40 cm s$^{-1}$ southwestward jet, extending from the base of the lower mixed layer (90–120 m) for 50 m, flowed through relatively quiescent waters above and below. This jet is seen as a layer of blue in the records of longitudinal and transverse velocity (Figs. 13b,c,e,f). The characteristic large-scale shear (0.50 m s$^{-1}$ over 50 m) is of order 0.01 s$^{-1}$. The finescale shears that bound the velocity layer are larger yet.

If the background shear is indeed the energy source, one might expect a preferential relationship between shear direction and wake orientation. In turn, if the solitons generate the wake, a relation between the direction of soliton propagation and that of the wake might be assumed. To investigate, ''background'' records of velocity and shear are formed by applying a 1-h running mean filter to the data. The high frequency wake is defined as the difference between the instantaneous and background fields. In Figs. 14a,c, the background and perturbation velocity vectors are plotted for a depth of 35 m. Axes are oriented such that a velocity in the direction of soliton propagation appears as an upward-pointing vector. Mean velocity vectors are plotted in red at 10-min intervals. The difference between the mean and instantaneous velocity, given by the blue vectors, is plotted at 2-min intervals. Successive vectors are offset to the right to indicate the passage of time.

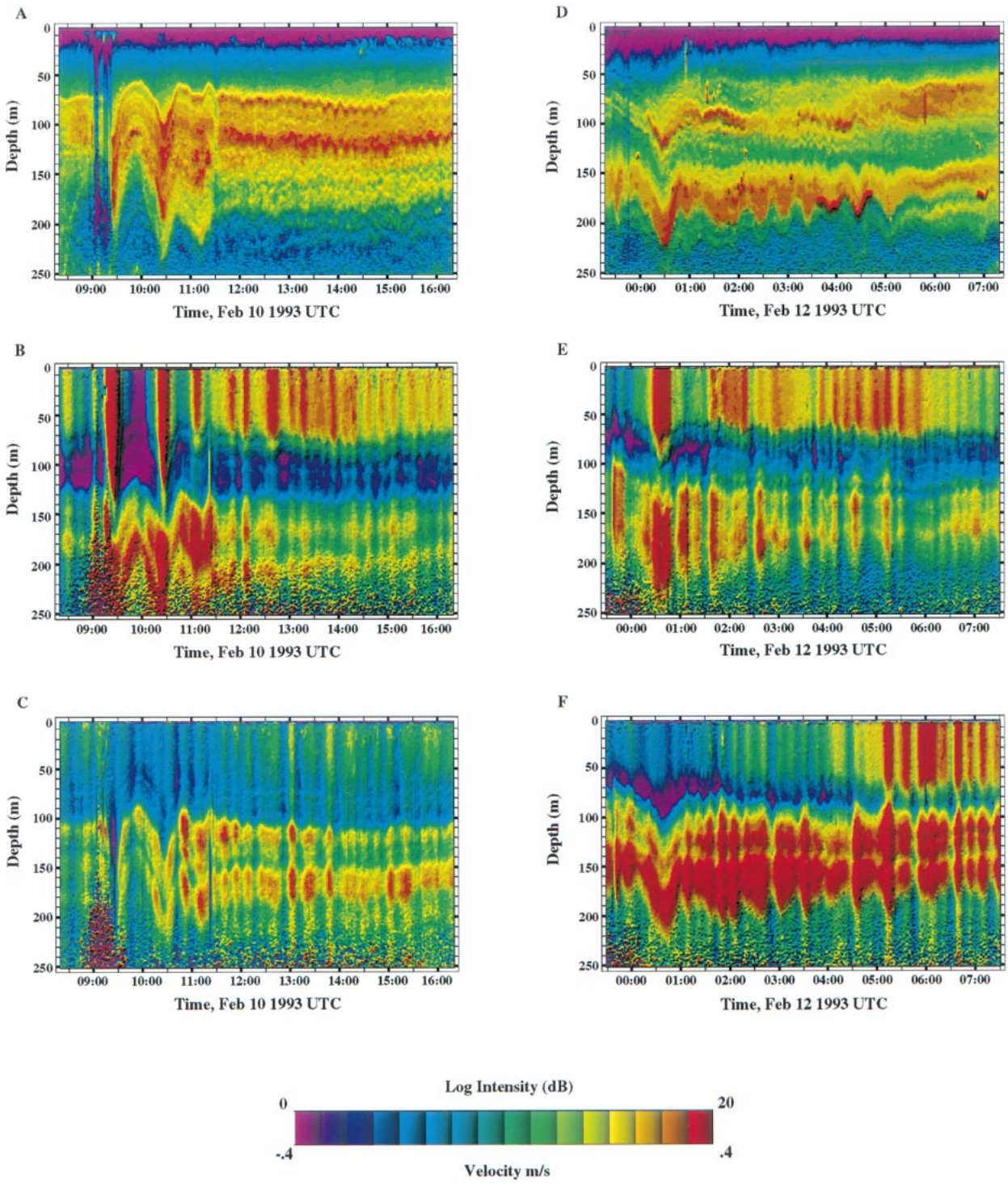


FIG. 13. (a) and (d) Acoustic scattering strength, (b) and (e) longitudinal, and (c) and (f) transverse velocity for the 10 and 12 Feb solitons. There is a marked increase in high-frequency low-mode internal wave activity in the hours following passage of the 10 Feb packet. In addition to the enhanced low mode activity, high mode ''interfacial'' waves are seen in the hours following passage of the 12 Feb event. The intensity scale in (a) and (d) varies over a factor of 100, rather than the factor of 30 in Fig. 6. Intensity increases are more difficult to detect in the nighttime data (10 Feb) vs daytime (12 Feb) as biological scattering levels increase at night.

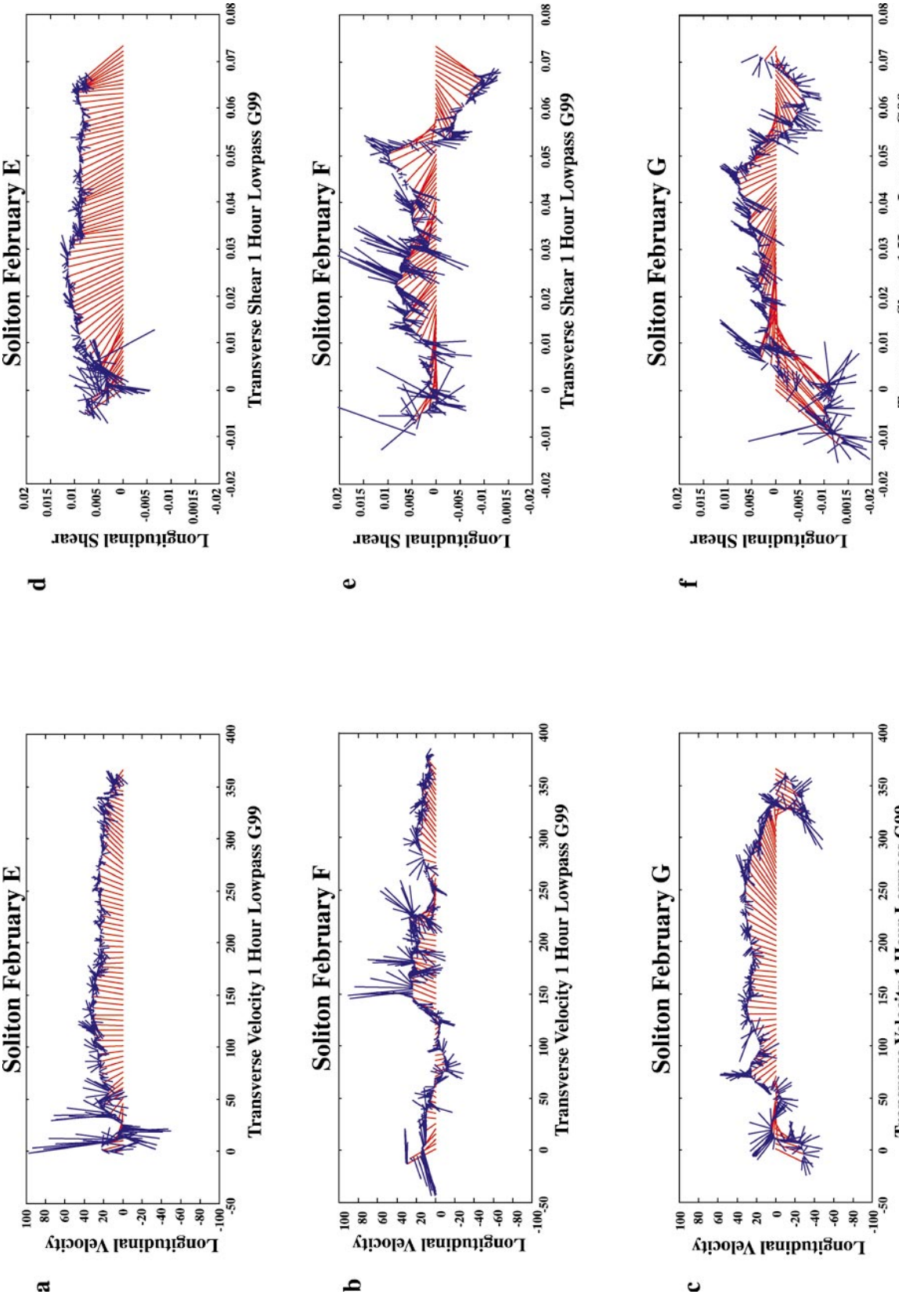


FIG. 14. (a), (b), (c) Velocity (10–40-m average) and (d), (e), (f) shear (50–100-m difference) during the passage of the 10–11 Feb events. Fields are presented in plan view as a sum of low-frequency (<1 cph, red) and residual (>1 cph, blue) components. Successive observations are offset to the right. Following the events, there is a clear preference for high-frequency shear fluctuations to orient normal to the low-frequency shear.

In the velocity records, the soliton arrival appears as a vertical pulse in the high-frequency signal. Subsequently, there is little relation between the high-frequency motions and the background. In contrast, high-frequency shear (Figs. 14d–f), taken as the velocity difference between 70 and 130 m, shows a marked preference in direction, being nearly orthogonal to the low-frequency shear background. Neither shear nor velocity signals appear to exhibit a preferred direction relative to the soliton propagation path.

It is perhaps not surprising that the high-frequency waves are oriented nearly orthogonal to the shear. The intrinsic phase speed of these waves is small compared to the typical velocity difference over the 50-m differencing interval. But if these waves are indeed orthogonal to the mean shear, how can they extract energy from it?

An upper bound rate of energy extraction is

$$\dot{E} = \rho\langle uw\rangle\left|\frac{\partial\overline{U}}{\partial z}\right| \quad [\text{W m}^3] \tag{19}$$

(Duda and Cox 1989). Here $\langle uw\rangle$ represents the wave Reynolds stress in the plane defined by the vertical (unit) vector and the background shear vector, $\partial\overline{U}/\partial z$. For waves not traveling in the direction of the mean shear this rate will be reduced.

The corresponding growth time for a wave of half-amplitude $\eta$ is

$$\tau = 0.5N^2\eta^2/\langle uw\rangle|\partial U/\partial z| \quad [\text{s}]. \tag{20}$$

For the present case, $N \cong 3.5 \times 10^{-5}$ s$^{-1}$, $\eta \cong 5$ m, and $\partial u/\partial z = 10^{-2}$ s$^{-1}$. An assumed Reynolds stress of order $\langle uw\rangle = 10^{-4}$–$10^{-5}$ m$^2$s$^{-2}$ yields growth times of 12–120 min, consistent with the observed growth of the low mode portion of the wakes.

The typical values of both $u$ and $w$ are adequate to provide this stress, provided that the growing waves have a slight component of propagation in the direction of the shear and that the $u$–$w$ correlation is large. In midgyre isotropic wave fields, the correlation has been found to be low (Ruddick and Joyce 1979; Plueddemann 1987). However, in the wake of the soliton, a few dominant packets are growing in a region that is initially relatively calm. Higher values of the correlation are possible.

If stresses of order $\langle uw\rangle = 10^{-4}$–$10^{-5}$ m$^2$ s$^{-2}$ are indeed being exerted in the upper thermocline, an associated eddy viscosity is of order

$$K_\nu = \langle uw\rangle/|\partial U/\partial z| = 10^{-2}\text{–}10^{-3} \quad [\text{m}^2\ \text{s}^{-1}]. \tag{21}$$

This huge (conjectured) drag would be active only during the period of wave growth, the first few hours following soliton passage.

If the event passage could be viewed in plan, the wake pattern might appear as a ''herringbone,'' with the long axis of the pattern oriented parallel to the mean shear, independent of soliton direction.[6] In spite of their rapid onset, the wake waves are oriented so as to minimally exchange energy with the mean shear. The ultimate size of the fastest growing waves, oriented more nearly parallel to the shear, is presumably limited by instability.

## 11. Summary

During the spring tides of late November, early January, and early February, groups of internal solitary waves propagated through the COARE domain. They travel northeastward at approximately 2.5 m s$^{-1}$ [as verified by radar, Pinkel et al. (1997)], closely coupled with the semidiurnal baroclinic tide. Peak amplitudes exceeded 60 m. Velocities in excess of 0.80 m s$^{-1}$ are seen.

The solitons are associated with the 5–7 largest crests of the spring tides. They appear phase-locked to the underlying tide, rather than evolving from the spread of a tidally induced random disturbance, as in Massachusetts Bay (Haury et al. 1979) or the Sulu Sea (Liu et al. 1985). (Given that we are within two mode-one wavelengths of the generation site, it is difficult to distinguish phase locking from simple concurrent generation.) Aspects of classical solitary wave behavior, solibore behavior, and parasitic instability are seen in the observations. The waves propagate through the strong shears of the equatorial current field with little apparent interaction.

Assuming that the flow is parallel to the propagation path during soliton passage and that the waveform evolves slowly in time, it is possible to calculate flow streamlines directly from the absolute velocity measurements. The streamlines track the observed vertical motion of scattering layers in advance of and during soliton passage. The agreement degrades in the hours following soliton passage, as the assumption of two-dimensionality loses validity.

The observed horizontal surface accelerations imply a horizontal pressure gradient that results from the vertical displacement of the sea surface. Displacements of 0.25 m maximum and slopes of $10^{-3}$ are implied. These estimates are consistent with the dynamic height calculations of Picaut et al. (1995) and Pinkel et al. (1997). Applying Bernoulli's relation, perturbation pressures can be calculated throughout the flow. From the pressure field (as well as straight from the velocity) it is seen that, while the vertical dependence of the solitons resembles the first baroclinic mode, the borelike aftermath is confined primarily to the upper 100 m. As solibore theory (Henyey and Hoering 1997) is extended from

[6] The pronounced three-dimensionality of the high-frequency wake invalidates the assumptions involved in our estimation of flow streamlines. Indeed, calculated streamlines have limited success in following the high-frequency wake.

two-layer to continuously stratified flows, this behavior must be incorporated.

The strong equatorial shears and the undercurrent itself are displaced both vertically and laterally by soliton passage. The tendency of the shear field to track material surfaces is a consequence of vorticity conservation. Shears transverse to the propagation path are perturbed by the along-path convergence associated with soliton passage. Upper ocean shears are initially reduced in magnitude and subsequently restored to their initial value. Deep ocean shears are amplified.

The solitary crests assume energy densities of 0.2 GJ $m^{-1}$, comparable to the underlying tide, within two (tidal) wavelengths of the suspected generation site. This implies an energy transfer rate of order 2 kW $m^{-1}$. Comparable growth rates are seen in the Sulu Sea observations (Apel et al. 1985), as well as in the numerical simulations of Liu et al. (1985) and Gerkema and Zimmerman (1995). This growth is ultimately limited by the radial spreading of the baroclinic waves or by dissipative processes.

With the flow streamlines, one can model the shear and strain of the soliton, as if the background equatorial current field were absent. The intrinsic shear associated with the COARE solitons is not sufficient to trigger Kelvin Helmholtz instability in a quiescent background. Minimum Richardson numbers remained above 15.

However, pronounced increases in acoustic scattering strength are seen following passage of all solitons. The suggestion is that the scattering is from index of refraction fluctuations. These may result from the overturning of the highly sheared background flow, which is triggered by the solitons. The salinity fine structure (0.46-cm scale) associated with Bragg backscattering at 160 kHz has a lifetime of hours, and forms a sort of acoustic dye that indicates the presence of breaking. While the dye appears to spread vertically throughout much of the upper thermocline, preexisting shear layers do not ''diffuse'' in concert. It is not appropriate to model this spread with any ''eddy viscosity.'' The apparent vertical ''mixing'' is presumably the result of extensive lateral spreading from distant overturning events.

The solitons of 10–12 February are associated with pronounced internal wave tails that develop in the hours following soliton passage. The waves appear to be oriented normal to the dominant background shear, independent of the direction of soliton travel. The suggestion is that the solitons trigger instability of the background shear. The observed rate of wave development suggests a large, though short-lived, eddy diffusivity, $K_\nu = 10^{-2}$–$10^{-3}$ $m^2$ $s^{-1}$, acting to reduce the shear.

The rapid development of high-frequency waves on the equatorial shear has been observed previously [see Mack and Hebert (1997) for a recent review]. In the eastern equatorial Pacific, where the undercurrent is shallower than in the COARE region, nocturnal convection is sufficient to trigger wave development.

In the aftermath of the 11–12 February event, several extremely high mode (vertical half-wavelength 80 m) nonlinear waves are observed. These are reminiscent of the interfacial solitons of Davis and Acrivos (1967) and represent a rare deep sea sighting of this phenomenon.

The velocity profiles of the solitons (January in particular) are not well-fit by second-order soliton models, given the coefficients of nonlinearity and dispersion appropriate for the site. The observed solitons are generally too broad. Excess breadth is a possible signature of cubic nonlinearity (Ostrovski and Stepanyants 1989; Lamb 1997) and has been seen in shallow water observations, as well (Stanton and Ostrovsky 1998). Lamb (1997) emphasizes that, as large solitons broaden, the associated mass flux and lateral displacement grows. These displacements can have consequence in the conduct of offshore operations and the functioning of offshore structures.

There appears to be a critical threshold for the development of solitons on the baroclinic tide. The variation in astronomic forcing between the spring tides associated with soliton formation and those that did not develop solitons is only 10%–20% (F98). (It might be that solitary wave behavior develops more often, but becomes visible only farther to the northeast, after the tidal crests pass the COARE site.) In the absence of soliton-like instability, the underlying tide often has a highly skewed waveform.

The long-term climatology of deep ocean solitary waves must be highly variable, changing with changing sea level over thousands of years, and with changing ocean basins geography and tidal strength over hundreds of millions of years.

*Acknowledgments.* The author thanks E. Slater, L. Green, M. Goldin, and C. Neely for the design, construction, and operation of the sonar system, as well as Capt. Schneible and the crew of the R.V. *John Vickers.* L. Washburn and D. Siegel graciously contributed the January CTD data used in this analysis. Contributions and comments from M. Merrifield, R. Weller, C. Eriksen, J. Picaut, M. McPhadden, and M. Alford, have been greatly appreciated. This work was supported by the TOGA program of the National Science Foundation under Grant NSF OCE 9110553.

## REFERENCES

Akylas, T. R., and R. H. Grimshaw, 1992: Solitary internal waves with oscillatory tails. *J. Fluid Mech.,* **242,** 279–298.

Apel, J. R., J. R. Holbrook, A. K. Liu, and J. J. Tsai, 1985: The Sulu Sea soliton experiment. *J. Phys. Oceanogr.,* **15,** 1625–1651.

Bogucki, D., and C. Garrett, 1993: A simple model for the shear-induced decay of an internal solitary wave. *J. Phys. Oceanogr.,* **23,** 1767–1776.

Bole, J. B., C. C. Ebbesmayer, and R. D. Romea, 1994: Soliton currents in the South China Sea: Measurements and theoretical modeling. *Proc. 28th Annual Offshore Technology Conf.,* Houston, TX, Marine Tech. Soc., 367–374.

Davis, R. E., and A. Acrivos, 1967: The stability of oscillatory internal waves. *J. Fluid Mech.,* **30-4,** 723–736.

Duda, T. M., and C. S. Cox, 1989: Vertical wavenumber spectra of velocity and shear at small internal waves scales. *J. Geophys. Res.,* **94,** 939–950.

Egbert, G. D., 1997: Tidal inversion: Interpolation and inference. *Progress in Oceanography,* Vol. 40, Pergamon Press, 53–80.

Feng, M., M. A. Merrifield, R. Pinkel, P. Hacker, A. J. Plueddemann, E. Firing, R. Lukas, and C. Eriksen, 1998: Semidiurnal tides observed in the western equatorial Pacific during the Tropical Ocean–Global Atmosphere Coupled Ocean–Atmosphere Response Experiment. *J. Geophys. Res.,* **103,** 10 253–10 272.

Fofonoff, N. P., 1969: Spectral characteristics of internal waves in the ocean. *Deep-Sea Res.,* **16** (Suppl.), 59–71.

Gerkema, T., and J. T. F. Zimmerman, 1995: Generation of nonlinear internal tides and solitary waves. *J. Phys. Oceanogr.,* **25,** 1081–1094.

Goodman, L., 1990: Acoustic scattering from ocean microstructure. *J. Geophys. Res.,* **95,** 11 557–11 573.

Gourdeau, L., 1998: Internal tides observed at 2°S–156°E by in-situ and TOPEX/POSEIDON data during the Coupled Ocean–Atmosphere Response Experiment (COARE). *J. Geophys. Res.,* **103** (C6), 12 629–12 638.

Haury, L. R., M. G. Briscoe, and M. H. Orr, 1979: Tidally generated internal wave packets in Massachusetts Bay. *Nature,* **278,** 312–317.

Henyey, F. S., and A. Hoering, 1997: Energetics of borelike internal waves. *J. Geophys. Res.,* **102** (C2), 3323–3330.

Joseph, R. I., 1977: Solitary waves in a finite depth fluid. *J. Phys. A. Math. Gen.,* **10,** L225–L227.

Korteweg, D. J., and G. de Vries, 1895: On the change of form of long wave advancing in a rectangular canal and on a new type of long stationary wave. *Phil. Mag., Ser 5,* **39,** 442.

Lamb, K. G., 1997: Particle transport by non breaking solitary internal waves. *J. Geophys. Res.,* **102** (C8), 18 641–18 660.

Lee, C. Y., and R. C. Beardsley, 1974: The generation of long nonlinear internal waves in a weakly stratified shear flow. *J. Geophys. Res.,* **79,** 453–462.

Liu, A. K., J. R. Hollbrook, and J. R. Apel, 1985: Non-linear internal wave evolution in the Sulu Sea. *J. Phys. Oceanogr.,* **15,** 1613–1624.

Lukas, R., and E. J. Lindstrom, 1991: The mixed layer in the western equatorial Pacific Ocean. *J. Geophys. Res.,* **96** (Suppl.), 3343–3357.

Mack, A. P., and D. Hebert, 1997: Internal gravity waves in the upper eastern equatorial Pacific: Observations and numerical solutions. *J. Geophys. Res,* **102** (C9), 21 081–21 100.

Miles, J., 1963: On the stability of heterogeneous shear flows. *J. Fluid Mech.,* **16,** 209–227.

Morozov, E. G., 1995: Semi diurnal internal wave global field. *Deep-Sea Res. I,* **42,** 135–148.

Ono, H., 1976: Algebraic solitary waves in stratified fluids. *J. Phys. Soc. Japan,* **39,** 1082–1091.

Osborne, A. R., and J. L. Burch, 1980: Internal solitons in the Andaman Sea. *Science,* **208,** 451–460.

Ostrovski, L. A., and Yu. A. Stepanyants, 1989: Do internal solitons exist in the ocean? *Rev. Geophys.,* **27,** 293–310.

Picaut, J., A. J. Busalachi, M. J. McPhaden, L. Gourdeau, F. I. Gonzalez, and E. C. Hacker, 1995: Open-ocean validation of TOPEX/POSEIDON sea level in the western equatorial Pacific. *J. Geophys. Res.,* **100,** 25 109–25 127.

Pinkel, R., and J. Smith, 1992: Repeat sequence codes for improved performance of Doppler sodar and sonar. *J. Atmos. Oceanic Technol.,* **9,** 149–163.

——, and S. Anderson, 1997: Shear, strain and Richardson number variations in the thermocline. Part I: Statistical description. *J. Phys. Oceanogr.,* **27,** 264–281.

——, M. Merrifield, M. McPhaden, J. Picaut, S. Rutledge, D. Siegel, and L. Washburn, 1997: Solitary waves in the western equatorial Pacific Ocean, *Geophys. Res. Lett.,* **24,** 1603–1606.

Plueddemann, A. J., 1987: Observations of the upper ocean using a multi beam Doppler sonar. Ph.D. thesis, University of California, San Diego, 183 pp.

Ray, R. D., B. V. Sanchez, and D. E. Cartwright, 1994: Some extensions to the response method of tidal analysis applied to TOPEX/Poseidon altimetry. *Eos, Trans. Amer. Geophys. Union,* **75** (Suppl.), 108.

Ruddick, B. R., and T. M. Joyce, 1979: Observations of interaction between the internal wavefield and low-frequency flows in the North Atlantic. *J. Phys. Oceanogr.,* **9,** 498–517.

Schrama, E. J. O., and R. D. Ray, 1994: A preliminary tidal analysis of TOPEX/Poseidon altimetry. *J. Geophys. Res.,* **99,** 24 799–24 808.

Seim, H., and M. Gregg, 1995: Acoustic backscatter from turbulent microstructure. *J. Atmos. Oceanic Technol.,* **12,** 367–380.

Sjoberg, B., and A. Stigebrandt, 1992: Computations of the geopgraphical distribution of the energy flux to mixing processes via internal tides and the associated vertical circulation of the ocean. *Deep-Sea Res.,* **39,** 269–292.

Stanton, T. P., and L. A. Ostrovski, 1998: Observations of highly nonlinear internal solitons over the continental shelf. *Geophys. Res. Lett.,* **25,** 2695–2698.

Thorpe, S. A., 1969: Neutral eigensolutions of the stability equation for stratified shear flow. *J. Fluid Mech.,* **36,** 673–683.

——, 1998: Nonlinear reflection of internal waves at a density discontinuity at the base of the mixed layer. *J. Phys. Oceanogr.,* **28,** 1853–1860.

——, and J. M. Brubaker, 1983: Observations of sound reflection by temperature microstructure. *Limnol. Oceanogr.,* **28,** 601–613.

Turner, J. S., 1973: *Buoyancy Effects in Fluid.* Cambridge University Press, 367 pp.

Webster, P. J., and R. Lukas, 1992: TOGA COARE: The Coupled Ocean–Atmosphere Response Experiment. *Bull. Amer. Meteor. Soc.,* **73,** 1377–1415.

Weller, R. A., and S. P. Anderson, 1996: Surface meteorology and air–sea fluxes in the western equatorial Pacific warm pool during TOGA COARE. *J. Climate,* **9,** 1959–1990.